Recovering signals in physiological systems with large datasets

Hodjat Pendar

Thesis submitted to the Faculty of the
Virginia Polytechnic Institute and State University
in partial fulfillment of the requirements for the degree of

Master of Science
in
Mathematics

Julianne Chung, Chair
Mark Embree
John J. Socha

August 14, 2020
Blacksburg, Virginia

Keywords: Inverse Problems, Signal Recovery, Respiration, Swimming, Flying

Recovering signals in physiological systems with large datasets

Hodjat Pendar

(ABSTRACT)

In many physiological studies, variables of interest are not directly accessible, requiring that they be estimated indirectly from noisy measured signals. Here, we introduce two empirical methods to estimate the true physiological signals from indirectly measured, noisy data. The first method is an extension of Tikhonov regularization to large-scale problems, using a sequential update approach. In the second method, we improve the conditioning of the problem by assuming that the input is uniform over a known time interval, and then we use a least-squares method to estimate the input. These methods were validated computationally and experimentally by applying them to flow-through respirometry data. Specifically, we infused CO_2 in a flow-through respirometry chamber in a known pattern, and used the methods to recover the known input from the recorded data. The results from these experiments indicate that these methods are capable of sub-second accuracy. We also applied the methods on respiratory data from a grasshopper to investigate the exact timing of abdominal pumping, spiracular opening, and CO_2 emission. The methods can be used more generally for input estimation of any linear system.

Recovering signals in physiological systems with large datasets

Hodjat Pendar

(GENERAL AUDIENCE ABSTRACT)

The goal of an inverse problem is to determine some signal or parameter of interest that is not directly accessible but can be obtained from an observed effect or a processed version that is measurable. Finding the gas exchange signal in animals is an example of an inverse problem. One method to noninvasively measure the gas exchange rate of animals is to put them in a respirometry chamber, flow air through the chamber, and measure the concentration of the respiratory gasses outside the chamber. However, because the gasses mix in the chamber and gradually flow through the gas analyzer, the pattern of the measured gas concentration can be dramatically different than the true pattern of real instantaneous gas exchange of the animal. In this thesis, we present two methods to recover the true signal from the recorded data (i.e., for inverse reconstruction), and we evaluate them computationally and experimentally.

Dedication

This work is dedicated to my father,

***Ebrahim Pendar**.*

May his memory be a blessing

Acknowledgments

I would like to express my deepest gratitude and acknowledgment to Dr. Julianne Chung for her insightful advice and compassionate support throughout this research. I sincerely appreciate her insight, guidance, kindness, and support. I would also like to extend my appreciation to my committee members, Dr. Mark Embree and Dr. Jake Socha for their valuable comments and help on my work.

Contents

List of Figures

List of Tables

Chapter 1

Introduction

Real-time measurements of endogenous and exogenous signals in living organisms are widely important in fields that span biology and medicine. However, the signals of interest are often not directly accessible, and their effect can only be measured indirectly. Hormone secretion, the rate of glucose utilization, oxygen consumption, and CO_2 production are just a few examples of such signals that cannot be directly measured [7, 17, 59]. A common approach to deal with this problem is to sample intermittently and then perform data fitting. For example, to determine hormone secretion or glucose production rate, blood concentration is repeatedly measured, and then rates are estimated from the recorded sequence [59]. However, the uncertainty of these estimates can be high due to the ill-conditioning of the systems. An ill-conditioned problem is an inherently unstable problem, where small errors in the data can lead to large errors in the solution, thereby making accurate estimation of the true signal very challenging [20, 26]. Measuring gas exchange in animals is an important example of indirect measurement of physiological signals. To determine the gas exchange rate of an animal using flow-through respirometry, the animal is put in a respirometry chamber and air is flowed through the chamber. The flowed air continuously replaces the consumed oxygen by the animal, washes out the CO_2 and water vapor produced by the animal, and brings the gasses to a gas analyzer. The pattern of measured gas concentration in the gas analyzer can be substantially different than the pattern of real instantaneous gas exchange of the animal, depending on the washout dynamics of the system [41, 42]. Any short burst of CO_2 gradually

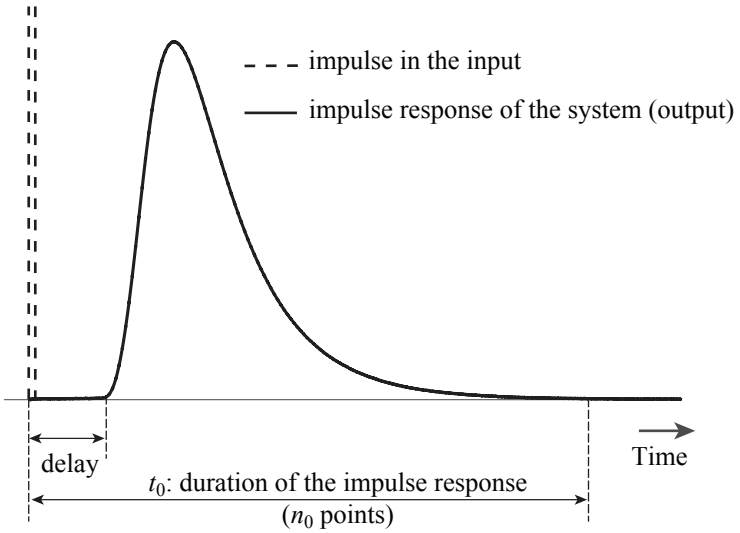

Figure 1.1: **Impulse response of the system.** When a short pulse of CO_2 is injected into the chamber and the concentration of the gas outside of the chamber is recorded with a gas analyzer, the shape of the output signal will be different from the input signal. This output signal is called the impulse response of the respirometry system.

leaves the respirometry system over the duration of a few seconds to several hours (Figure 1.1). During this time interval, the short burst can also be combined with other CO_2 bursts. Therefore, interpretations of physiological function based on raw respiratory data can be misleading [24], and can become even more problematic if the respiratory signal has to be synched with another real-time and rapidly changing signal, such as pressure, movement, or temperature.

Generally, these physiological measurement problems, in addition to many other unrelated scientific applications such as image de-blurring and 3D tomographic reconstruction, are referred to as 'input-estimation' or 'inverse problems' [13, 14, 16, 17]. In an input estimation problem, the signal of interest, represented by the input signal $u(t)$, is not available, but a transformation or convolution of $u(t)$, called the output signal $y(t)$, is measurable. Assuming that the system is linear and time-invariant, the output signal ($y(t)$) can be written as a convolution of the input signal ($u(t)$) and the impulse response of the system [30]:

$$y(t) = \int_0^t \hat{h}(t-\tau)u(\tau)d\tau, \tag{1.1}$$

where $y(t)$ is the output of the system at time t, which is measured by the gas analyzer. $\hat{h}(t)$ is the impulse response of the system, which can be found experimentally (Figure 1.1). Given the output $y(t)$ and the impulse response function $\hat{h}$, we aim to recover u, which is the true gas exchange signal from the animal. In practice, we consider the discrete form of the convolution equation (1.1), which is given by:

$$y_k = \sum_{i=0}^{k} h_{k-i}u_i, \tag{1.2}$$

where y_k and u_k describe the average of the output and input respectively, when $k\delta t \leq t \leq (k+1)\delta t$, δt is the sampling interval, and $h(k)$ is the integral of $\hat{h}(t)$ in the sampling period, i.e.,

$$h_k = \int_{k\delta t}^{(k+1)\delta t} \hat{h}(\tau)d\tau. \tag{1.3}$$

Using matrix and vector notation, the discrete convolution equation (1.2) can be represented using the matrix equation:

$$\bar{\mathbf{y}} = \mathbf{H}\mathbf{u}, \tag{1.4}$$

where $\bar{\mathbf{y}} = (y_0 \;\; y_1 \;\; \dots \;\; y_n)^T$ is the output of the system (with no noise), $\mathbf{u} = (u_0 \;\; u_1 \;\; \dots \;\; u_n)^T$ is the desired, unknown input, and

$$\mathbf{H} = \begin{pmatrix} h_0 & 0 & \cdots & 0 \\ h_1 & h_0 & \cdots & 0 \\ \vdots & \vdots & \ddots & \vdots \\ h_n & h_{n-1} & \cdots & h_0 \end{pmatrix} \tag{1.5}$$

is an $(n+1) \times (n+1)$ lower triangular matrix that models the forward convolution process underlying respirometry. Notice that solving the inverse problem for respirometry requires solving a system of linear equations (1.4), so standard techniques from numerical linear algebra could be used. However, solving this system is not trivial due to the ill-posedness of the underlying problem [46]. This is revealed in the inherent singularity and poor conditioning of the coefficient matrix $\mathbf{H}$. Furthermore, the solution is very sensitive to noise in the measured data and computational errors [17]. That is, in practical situations, there is a small amount of error or noise in the data, and the model is given by

$$\mathbf{y} = \mathbf{H}\mathbf{u} + \mathbf{e}, \tag{1.6}$$

where $\mathbf{e}$ represents unknown noise or errors in the observed data. Due to ill-posedness, these small errors in the data can lead to large errors in the solution, and the inverse solution $\mathbf{H}^{-1}\mathbf{y}$ is useless. Regularization methods have been proposed to remedy ill-conditioning by solving a related problem that is both uniquely solvable and robust to noise [20, 26]. Tikhonov regularization is a well-known and widely used approach to solve such inverse problems [22]. However, efficient implementations for very large datasets, such as when measurements are taken frequently and/or over long time intervals, are challenging. In this thesis, we propose two approaches for extending Tikhonov regularization to large datasets. First, we take advantage of the small duration of the impulse response relative to the size of the dataset to partition the dataset and apply the Tikhonov method in a sequential manner. Second, we introduce a dimension reduction approach to regularization that reduces the ill-conditioning of the system and uses an averaging of least-squares solutions to recover the inputs of the original system.

1.1 Tikhonov regularization method

Tikhonov regularization has been used to solve a variety of inverse problems such as image de-blurring, tomographic reconstruction, and estimation of gas exchange [14, 17, 57, 61]. Although other methods such as trend-identification, Kalman filtering, and Kalman smoothing can be used for input estimation, the Tikhonov method is often preferred for its better performance in gas exchange problems, for example in studies with whole-room calorimeters [57]. The Tikhonov solution to the inverse problem (1.6) is given by

$$\hat{\mathbf{u}} = \text{argmin}_u\{\|\mathbf{y} - \mathbf{H}\mathbf{u}\|^2 + \gamma\|\mathbf{Q}\mathbf{u}\|^2\}, \tag{1.7}$$

where $\gamma > 0$ is a regularization parameter and $\mathbf{Q}$ is a design or regularization matrix that enforces smoothness of the solution. The first term on the right side of (1.7) is the data fit term, which measures how loyal the estimate is to the data, and the second term penalizes roughness of the solution. The amount of penalization is controlled by the choice of the regularization parameter γ, and a common choice of the regularization term is where $\mathbf{Q}\mathbf{u}$ represents the discrete derivative of $\mathbf{u}$. Therefore, the Tikhonov regularized solution (1.7) tends to be smooth. One nice feature of Tikhonov regularization is that there exists a closed-form solution given by

$$\hat{\mathbf{u}} = \mathbf{M}\mathbf{y}, \tag{1.8}$$

where

$$\mathbf{M} = (\mathbf{H}^T\mathbf{H} + \gamma\mathbf{Q}^T\mathbf{Q})^{-1}\mathbf{H}^T. \tag{1.9}$$

The regularization parameter γ plays an important role in the quality of the Tikhonov

solution and is typically tuned via an experimental calibration. A large value of γ puts more emphasis on the regularization term and makes the solution smoother, thereby preventing the solution from being corrupted by inverted noise. On the other hand, a small value of γ puts less weight on the regularization term, and the solution resembles the noise-contaminated inverse solution. Various methods have been proposed to choose γ, such as the discrepancy principle, the L-curve, the unbiased predictive risk estimator, and the generalized cross-validation method [17, 26, 32]. Some of these methods require prior knowledge about the noise and the noise level. There is also a variety of choices for the regularization matrix $\mathbf{Q}$ [17, 57]. In this area, the most common choices for $\mathbf{Q}$ include the identity matrix ($\mathbf{Q} = \mathbf{I}$) or a discretization of the derivative operator. For example, for respirometry, $\mathbf{Q}$ can be a lower triangular Toeplitz matrix, where the first column is given by $(1 \quad -2 \quad 1 \quad 0 \quad \cdots \quad 0)^T$, which penalizes the sum of squared second differences. If penalizing the second difference causes excessive smoothness (e.g., the estimation loses sharp changes in the input), $\mathbf{Q}$ can be chosen to be a lower triangular Toeplitz matrix, where the first column is $(1 \quad -1 \quad 0 \quad \cdots \quad 0)^T$, corresponding to the first difference of the estimation.

1.2 Overview of Contributions and Outline

In this thesis, we investigate extensions of the Tikhonov regularization method for large-scale problems arising in respirometry signal reconstruction. Two new methods were developed to recover physiological signals from large datasets. The methods were evaluated numerically and experimentally, with both methods showing sub-second accuracy in recovering respiratory signals, and the developed methods were used in real biological studies. Using the methods we showed that sometimes the respiratory system of locusts acts as a unidirectional pump. This work is published in [51].

An overview of this thesis is as follows. In Chapter 2 we describe two new methods for input estimation. The first method is based on exploiting overlapping regions and the second method is based on dimension reduction techniques. Numerical and experimental evaluation of the proposed methods along with a biological case study are provided in Chapter 3, and a discussion of methods is provided in Chapter 4.

Chapter 2

New methods for input estimation

In this chapter, we introduce two new methods for input estimation for solving the respirometry inverse reconstruction problem.

2.1 Method I - Extension of the Tikhonov method for large datasets

For very large datasets, computing the Tikhonov solution as in Equations (1.7) and (1.8) may be computationally infeasible. In particular, because the dimensions of matrix $\mathbf{H}$ correspond to the size of the data vector, constructing and storing $\mathbf{H}$ and computations with $\mathbf{H}$ may be burdensome and expensive. Iterative methods may provide an alternative approach for large, sparse linear systems, but preconditioning may be required for fast convergence. Instead, we propose to apply the Tikhonov method to smaller fragments or partitions of the data, while being attentive to the overlapping regions. From the impulse response function, we know that any input signal, such as a short burst of CO_2, will contribute to future output/measurements for the duration of t_0, meaning for n_0 data points (Figure 1.1). Therefore, the input between 0 to t (n data points) affects the output from 0 to $t + t_0$ ($n + n_0$ data points). To recover the input, we propose the following algorithm:

Step 1: Consider the first $n_0 + n$ data points and construct corresponding matrices $\mathbf{H}$, $\mathbf{Q}$,

and $\mathbf{M} = (\mathbf{H}^T\mathbf{H} + \gamma\mathbf{Q}^T\mathbf{Q})^{-1}\mathbf{H}^T$. Notice that these are small matrices of size $n + n_0$, so the inverse or matrix factorizations (e.g., QR or LU) can be easily computed.

Step 2: Use Equation (1.8) to estimate the $n + n_0$ inputs from the first $n + n_0$ data points ($\mathbf{y}$). Because the last n_0 input points affect the output points that are not included in the first $n + n_0$ output points, only accept and record the first n inputs or less, and disregard the rest of the estimated inputs.

Step 3: To deal with overlapping regions, use Equation (1.2) or Equation (1.4) to determine the corresponding output for the first n estimated inputs, and then subtract it from the data vector $\mathbf{y}$. Eliminate the first n points of the new $\mathbf{y}$ vector and repeat the sequence from step 2 again.

This algorithm does not determine all the inputs at once, but rather estimates n points of the input at each cycle. The computational advantages of this algorithm are 1) it breaks the problem into smaller problems, thereby avoiding to solve a very large system of equations, and 2) for equally spaced partitions, matrix $\mathbf{M}$ or an efficient representation of $\mathbf{M}$ only needs to be computed once. The main computational cost per cycle is a simple linear solve, which is very cheap. We remark that for equally spaced partitions, a matrix factorization of matrix M can be calculated once and re-used in all subsequent steps for efficient computational implementation. The regularization parameter γ must be determined experimentally for each custom setup.

2.2 Method II - Dimension reduction method

Another approach to deal with ill-conditioning or the singularity of $\mathbf{H}$ is to use a projection approach or dimension reduction technique. The basic idea is the assumption that the solu-

tion lies in a low-dimensional subspace, which has a regularizing effect on the problem (i.e., eliminating the singularity and/or significantly improving the conditioning of the problem). Here, assume that m consecutive points in the input signal are equal:

$$\mathbf{u}(i) = \bar{u}_j, \qquad (m-1)j \leq i \leq mj. \tag{2.1}$$

If we assume, without loss of generality, that the number of data points $N = mn$, then the projected problem has the form,

$$\min_{\bar{u}}\{\|\mathbf{y} - \mathbf{HL}\bar{\mathbf{u}}\|^2\}, \tag{2.2}$$

where $\mathbf{u} = (\bar{u}_1\ \bar{u}_2\ ...\ \bar{u}_n)^T$ is an $n \gg 1$ vector and $\mathbf{L}$ is a $N \gg n$ matrix with the following elements:

$$\mathbf{L}_{ij} = \begin{cases} 1, & m(j-1)+1 \leq i \leq mj; \\ 0, & \text{otherwise.} \end{cases} \tag{2.3}$$

Because of the added constraint on the input vector, the projected problem is better conditioned than the original problem (see Appendix A for details), and Equation (2.1) can be solved using any least-squares method for over-determined systems of equations, because $\mathbf{HL}$ has full column rank. In summary, the solution in the original space is given by

$$\mathbf{u} = \mathbf{My}, \tag{2.4}$$

where

$$\mathbf{M} = \mathbf{L}(\mathbf{L}^T\mathbf{H}^T\mathbf{HL})^{-1}\mathbf{L}^T\mathbf{H}^T. \tag{2.5}$$

Because we have assumed that m consecutive input points are equal, the solution in Equation (2.4) cannot track input changes within these intervals, and false artifacts such as sharp jumps between intervals are introduced as a consequence of this assumption. To improve the accuracy of the solution and to obtain a smoother representation, we slide the interval m times in increments of 1, each time computing an estimate of the input, and we take the final solution to be the average of these m solutions. More precisely, let $1 \leq k \leq m$ and let $\mathbf{P}_k$ be a lower shift matrix whose $(i,j)^{th}$ component is: $(\mathbf{P}_k)_{ij} = \delta_{i,j+k-1}$, where δ is the Kronecker delta. For example, $\mathbf{P}_k\mathbf{X}$ shifts the components of vector $\mathbf{X}$ down by k element and introduces a zero in the first k elements, whereas $\mathbf{P}_k^T\mathbf{X}$ shifts the components of vector $\mathbf{X}$ up by k element and introduces a zero in the last k elements. Then, for each k, a solution can be computed as

$$\mathbf{u}_k = \mathbf{P}_k^T\mathbf{M}\mathbf{P}_k\mathbf{y}, \tag{2.6}$$

where $\mathbf{M}$ is defined in Equation (2.5). By linearity, the average of all m solutions is given by

$$\hat{\mathbf{u}} = \tilde{\mathbf{M}}\mathbf{y}, \tag{2.7}$$

where

$$\tilde{\mathbf{M}} = \frac{1}{m}\sum_{k=1}^{m}\mathbf{P}_k^T\mathbf{M}\mathbf{P}_k. \tag{2.8}$$

Thus, each reconstruction matrix is just a shifted submatrix of the original matrix, and important spectral properties can be shown (see Appendix A for details). For extremely large data sets, we can combine the dimension reduction approach with the partitioning approach described in method I. That is, we can apply this method on $n + n_0$ data points, accept only the first n estimated inputs, find the corresponding output of the n estimated input points, and subtract it from the vector y. Then, we eliminate the first n points of the data and repeat the procedure for the next $n + n_0$ data points.

Chapter 3

Evaluation of the methods

The new methods presented in this thesis were evaluated both on simulated and experimental datasets.

3.0.1 Numerical experiments and validation

A MATLAB code was written to model a flow-through respirometry system using Equation (1.1). This code determines the output ($\mathbf{y}$) of the respirometry system for any given input ($\mathbf{u}$) and impulse response ($\hat{\mathbf{h}}$). We used the impulse responses of a rectangular 28 mL flow-through respirometry chamber model with inlet flow rates of 250 and 500 mL/min, which were determined experimentally in a previous study [50]. The input was considered to be sequences of three rectangular pulses with different frequencies of 0.1, 0.2, 0.5, 1 and 2 Hz (Figures 3.1 and 3.2). The simulation was repeated by adding 0.01%, 0.1%, 1%, 2%, 5%, and 10% normally-distributed noise to the output. The sampling rate of the signals was assumed to be 10 Hz, with the duration of the virtual experiment of one hour (36,000 data points). Both methods were used to recover the input from the output signal. Because the size of the dataset was large, we applied both methods to the data points, $n + n_0 = 1500$, at each iteration ($n_0 = 720$, Figure 1.1). The recovered inputs were compared with the true input at each frequency and each noise level separately.

3.1 Experimental validation

To test the methods experimentally, we used a high-speed valve (MHE2-MS1H-5/2-M7-K, Festo, NY, USA) to switch between 100 ppm CO_2 gas (100 ppm, balanced with N_2) and regular air immediately before a 28 mL (25×25×45 mm3) respirometry chamber similar to the simulation setup. The experiment was repeated with two inlet flow rates of 250 mL/min and 500 mL/min. Data were recorded for one hour with a sampling rate of 10 Hz. Both reconstruction methods were applied to the recorded data to recover the original CO_2 infusing pattern. The details of the experimental setup are described in [50].

3.2 Case study: abdominal pumping, spiracular control, and CO_2 emission in a grasshopper

In insects, air enters the body through valves called spiracles, and then is directly delivered to the tissues through a complex network of tracheal tubes. The same system is used to transport CO_2 from the tissues to the surrounding air. Gas transport occurs via mixed diffusion and advective flows [56]. These flows can be created by compression of the tracheal system, which can be linked to abdominal pumping and an increase in hemolymph (blood) pressure [49]. The pattern of airflow can also be affected by the spiracular valve timing. Thus, studying the coordination of abdominal pumping, hemolymph pressure, the status of spiracles, and CO_2 emission is essential to understanding how insects actively breathe. However, the recorded data depends on many parameters of the experimental respirometry system, including flow rate, chamber volume, length of tubing, and internal structure of the gas analyzer, and emitted CO_2 signals are not captured independently and in real time

[42, 50]. In contrast, hemolymph pressure, the status of the spiracles, and the movement of the abdomen can be measured or observed directly and in real time. To synchronize these signals, it is necessary to recover the instantaneous gas exchange from the CO_2 record. Because the dynamics of the hemolymph pressure, abdominal movement, and spiracles can be fast, the instantaneous gas exchange must be determined with high temporal accuracy to be synched with other signals. Otherwise, timing patterns may be misinterpreted. As a demonstration of the effectiveness of our methods on a real system, we measured the CO_2 production rate of a male grasshopper (*Schistocerca americana*; mass = 1340 mg) in a flow-through respirometry system at room temperature (22C). For these measurements, the grasshopper was placed in a 28 mL chamber and CO_2–free air was flowed in at rate of 500 mL/min; emitted CO_2 was recorded with an infrared gas analyzer (LI 7000 Li-Cor, Nebraska, USA). The abdominal movements and the movements of the second thoracic spiracle on the left side of the body were also recorded with a video camera (NEX-VG10, Sony) at 30 frames per second. A total of 12 minutes were recorded, representing 100 abdominal pumping cycles. To determine the impulse response of the system, a simple model of the animal was made with adhesive putty and was placed inside the chamber. A short pulse of 100 ppm CO_2 (duration, 200 ms) was injected into the chamber. The output of the gas analyzer was recorded and normalized to determine the impulse response of the system [50]. Lastly, we used the impulse response to define the forward model H and used it in both methods to recover the instantaneous CO_2 emission of the animal. The mesothoracic spiracles of grasshoppers are externally visible, so it was possible to determine the open/closed status of this spiracle from the video records (Figure 3.5). The lip-like spiracle contains two moving parts, the atrial lips, which together act as a valve. Using Quicktime software, video of the thoracic spiracle (movie 1) was analyzed frame-by-frame to determine the open/closed status of the spiracle. Any frames that indicated a gap between the lips were coded as ‘open’. Correspondingly, when there was no gap between the lips, the frames were coded as ‘closed’.

To determine the abdominal movement, we used a custom MATLAB code to track one point on the ventral cuticle frame by frame in the same movie. To synchronize the video data with the CO_2 data, we first recorded a pulse of light initiated by a voltage pulse from the data acquisition system, and then aligned the signals post-hoc.

3.3 Results

3.3.1 Numerical experiments and validation

The input signals were recovered using both methods and compared with the true input signal. The results of both methods are very similar (Figures 3.1 and 3.2 and Tables 3.1 and 3.2). By increasing the input frequency and noise, the accuracy of the methods decreased. The methods captured pulses with durations down to 0.5 s in the higher flow rate (F = 500 mL/min), but only when the noise was less than 0.1% (Figure 3.1). Both methods recovered the pulses with durations down to 2 s when the noise level was up to 5%, which is a very high value. In the higher flow rate, the 2 s pulses were recovered even with a high noise level of 10% (Figures 3.1 and 3.2; see Appendix C for more detail). In general, by decreasing the tuning parameters (γ in Tikhonov method and m in dimension reduction method), it is possible to recover even higher frequency inputs; however, the results become noisier. The Pearson correlation coefficient of the recovered signals and the true signals varied by noise level (Table 3.1 and 3.2), and these numbers further indicate that both methods perform very closely.

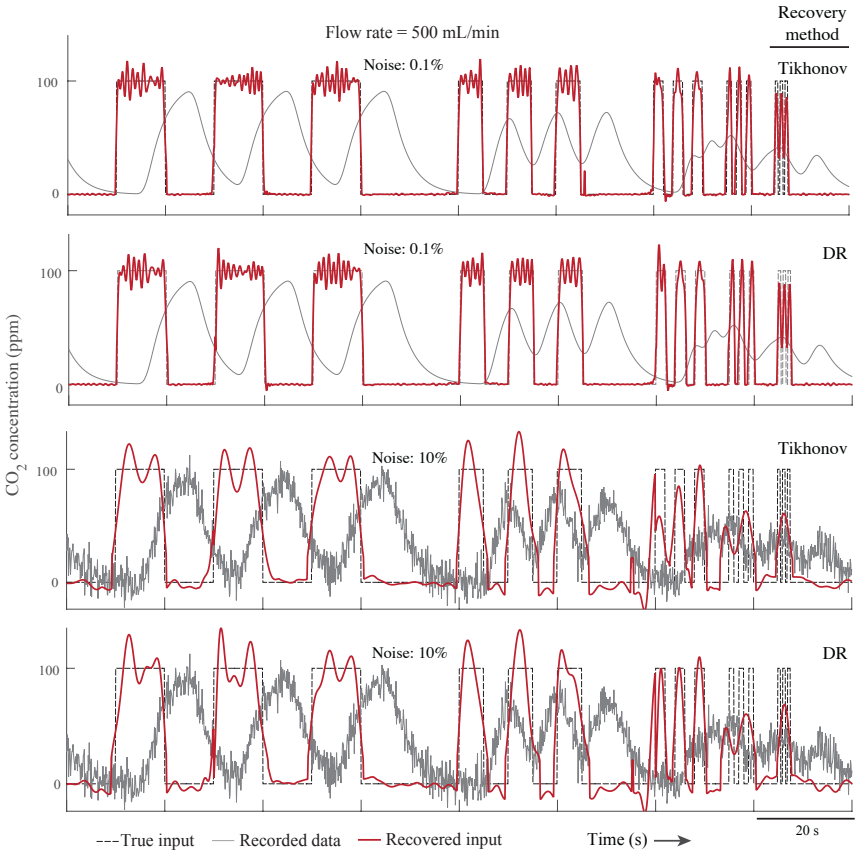

Figure 3.1: **Simulation results (flow rate: 500 ml/min).** Both Tikhonov and dimension reduction (DR) methods were able to recover fast changes in the input (1 Hz or 0.5 s pulses) when the noise level is low. With extremely noisy data (10%), the methods were able to recover pulses with duration of 2 s.

3.3.2 Experimental validation

The noise level of the respirometry system was measured to be 0.014%, determined by recording the CO_2 concentration using the same methodology, but with an empty chamber. The estimations of instantaneous gas exchange rate from both methods are very similar (Figures 3.3 and 3.4). The Pearson correlation coefficients between the recovered signal and the true signal for different input frequencies, different flow rates, and signal recovery methods were calculated separately (Tables 3.1 and 3.2). The difference between the Pearson

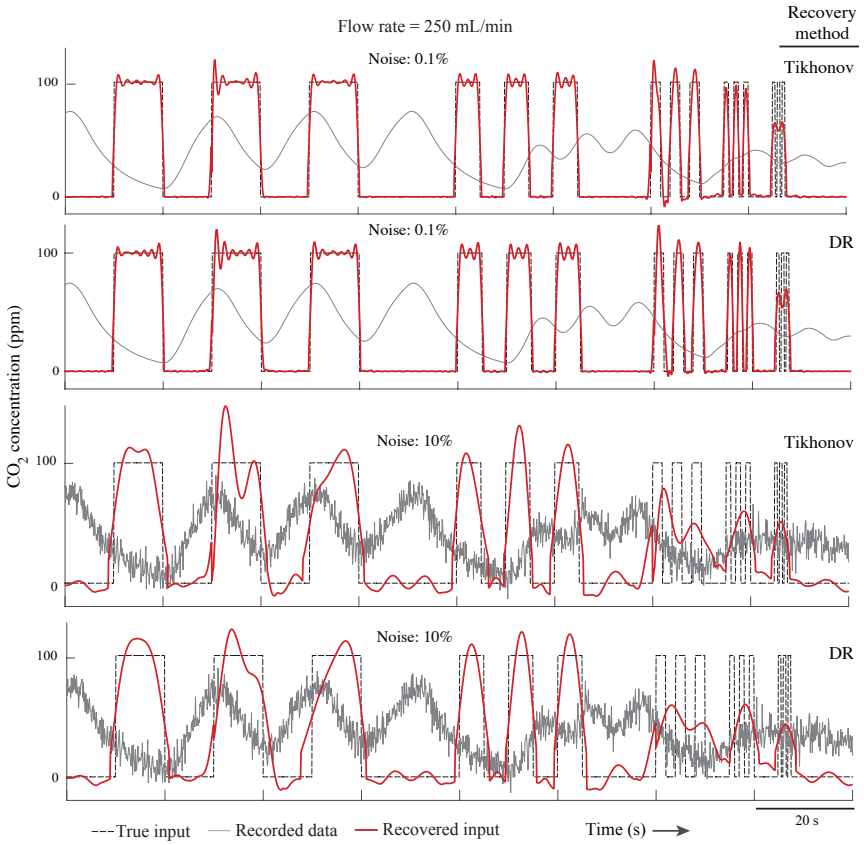

Figure 3.2: **Simulation results (flow rate: 250 ml/min).** When the noise level was low, the methods recovered the inputs with the frequency of 0.5 Hz (pulse duration of 1 s). With extremely noisy data (10%) the methods recovered 0.1 Hz (pulse duration of 5 s) input signals.

correlation coefficients for the two methods is 0.02% on average. Both methods were able to recover pulses with duration of 0.5 s in both flow rates; however, both were more accurate with the higher flow rate of 500 mL/min (Figures 3.3 and 3.4 and Table 3.3).

Table 3.1: Pearson correlation coefficient between the true and the recovered input using the Tikhonov method (simulation study)

		F = 500 mL/min						F = 250 mL/min					
Noise (%):		0.01	0.1	1	2	5	10	0.01	0.1	1	2	5	10
Regulation parameter		1e-5	2e-4	0.06	0.1	1.4	4.1	05e-4	0.02	0.4	0.85	4.5	15
Pulse duration (s)	10	0.989	0.985	0.979	0.973	0.969	0.969	0.986	0.981	0.973	0.966	0.951	0.945
	5	0.979	0.972	0.962	0.956	0.933	0.933	0.969	0.964	0.959	0.930	0.926	0.887
	2	0.962	0.928	0.929	0.926	0.873	0.873	0.923	0.929	0.914	0.872	0.715	0.420
	1	0.921	0.918	0.564	0.505	0.496	0.496	0.913	0.566	0.525	0.492	0.494	0.213
	0.5	0.861	0.541	0.467	0.469	0.463	0.478	0.564	0.483	0.472	0.479	0.462	0.410

3.3.3 Case study: abdominal pumping, spiracular control, and CO_2 emission in grasshopper (*Schistocerca americana*)

The duration of the abdominal pumps and CO_2 bursts of the grasshopper were 1.9±0.4 s and 1.1±0.3 s, respectively. Most abdominal pumps (67.4%) were followed by the opening of the thoracic spiracle. All openings of the thoracic spiracle started when the abdomen began to relax at the end of the abdominal pump. In contrast, the spiracle was closed during the start of the pump cycle. The duration of the spiracle's open phase was 0.5±0.1 s (mean ± SD). The raw data of the CO_2 emission show a continuous pattern of gas exchange. However, the corrected CO_2 emission signal reveals that the animal was exhibiting discontinuous gas exchange (Figure 3.5) with periods of thoracic spiracular closure, followed by bursts of CO_2 release. All CO_2 bursts coincided with abdominal pumps on a one-to-one basis. The correlation coefficient of the abdominal movement and the raw CO_2 signal was 0.376; however, after recovering the true CO_2 signal, this value increased to 0.73. There were also some abdominal pumps and CO_2 bursts observed that were not followed by the opening of the spiracle (28.4%). Based on the raw CO_2 signal, only 44.7% of the CO_2 was emitted during

Table 3.2: Pearson correlation coefficient between the true and the recovered input using the dimension reduction method (simulation study)

		F = 500 mL/min						F = 250 mL/min					
Noise (%):		0.01	0.1	1	2	5	10	0.01	0.1	1	2	5	10
Regulation parameter		5	10	13	15	19	20	7	13	17	20	22	35
Pulse duration (s)	10	0.989	0.985	0.975	0.972	0.968	0.966	0.986	0.981	0.977	0.972	0.964	0.946
	5	0.977	0.972	0.962	0.959	0.931	0.892	0.988	0.965	0.953	0.939	0.935	0.928
	2	0.958	0.904	0.928	0.922	0.827	0.806	0.969	0.929	0.923	0.866	0.811	0.443
	1	0.921	0.875	0.530	0.479	0.436	0.494	0.924	0.591	0.517	0.499	0.504	0.336
	0.5	0.823	0.534	0.474	0.471	0.464	0.472	0.926	0.488	0.477	0.478	0.464	0.407

abdominal pumping; however, the corrected CO_2 signal shows that 76.5% of the CO_2 was released during abdominal pumping. There was only a small amount of CO_2 emitted during the opening phase of the thoracic spiracle (8.6%), and most of the CO_2 was released when the spiracle was closed.

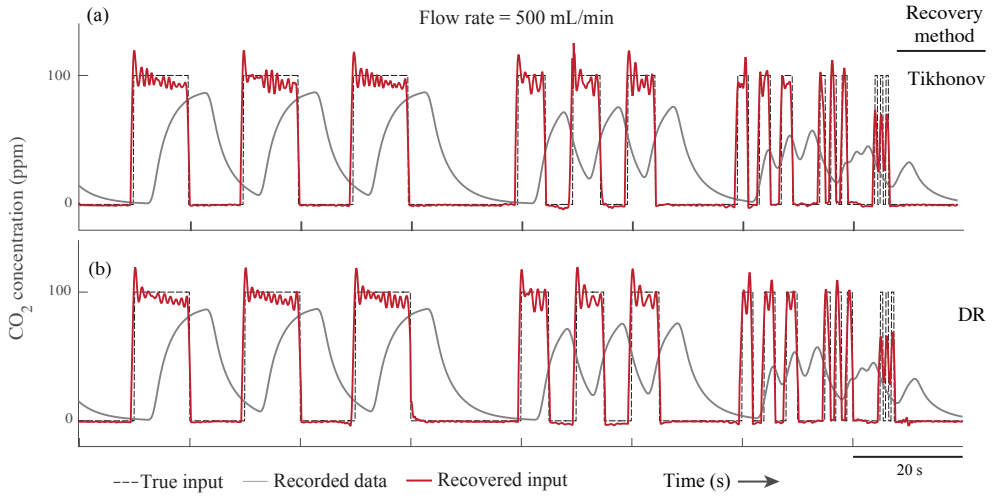

Figure 3.3: **Experimental results (flow rate: 500 ml/min).** Both Tikhonov and dimension reduction (DR) methods were able to recover fast changes in the input with the frequency of 1 Hz or pulse duration of 0.5 s.

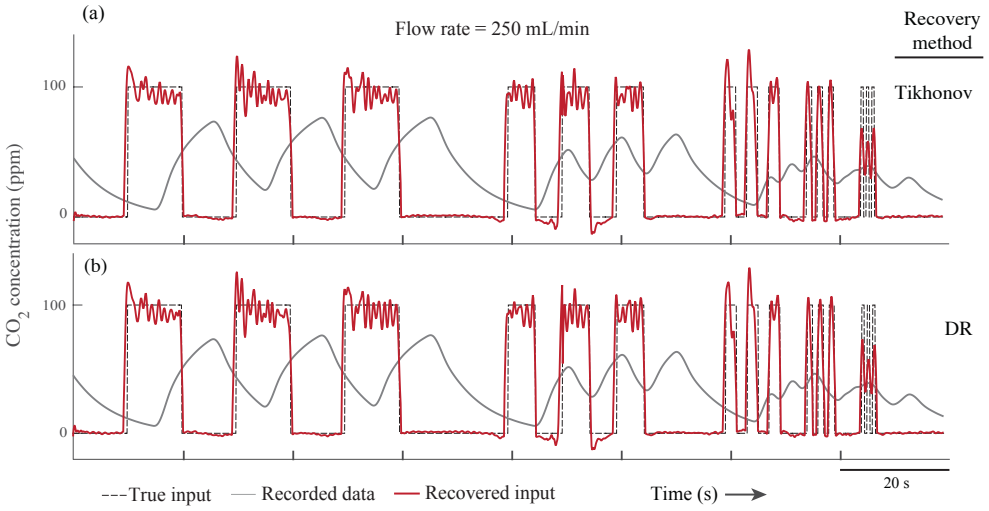

Figure 3.4: **Experimental results (flow rate: 250 ml/min).** Even in this lower flow rate, both Tikhonov and dimension reduction (DR) methods successfully recovered the fast changes in the input (frequency of 1 Hz).

Table 3.3: Pearson correlation coefficient between the true and the recovered input using the Tikhonov and dimension reduction method for experimental data

		Tikhonov		Dimension Reduction	
Flow rate (mL/min)		250	500	250	500
Regulation parameter		2e-5	1e-5	5	4
Pulse duration (s)	10	0.969	0.960	0.967	0.962
	5	0.961	0.927	0.966	0.925
	2	0.938	0.886	0.930	0.884
	1	0.803	0.818	0.811	0.816
	0.5	0.699	0.661	0.709	0.685

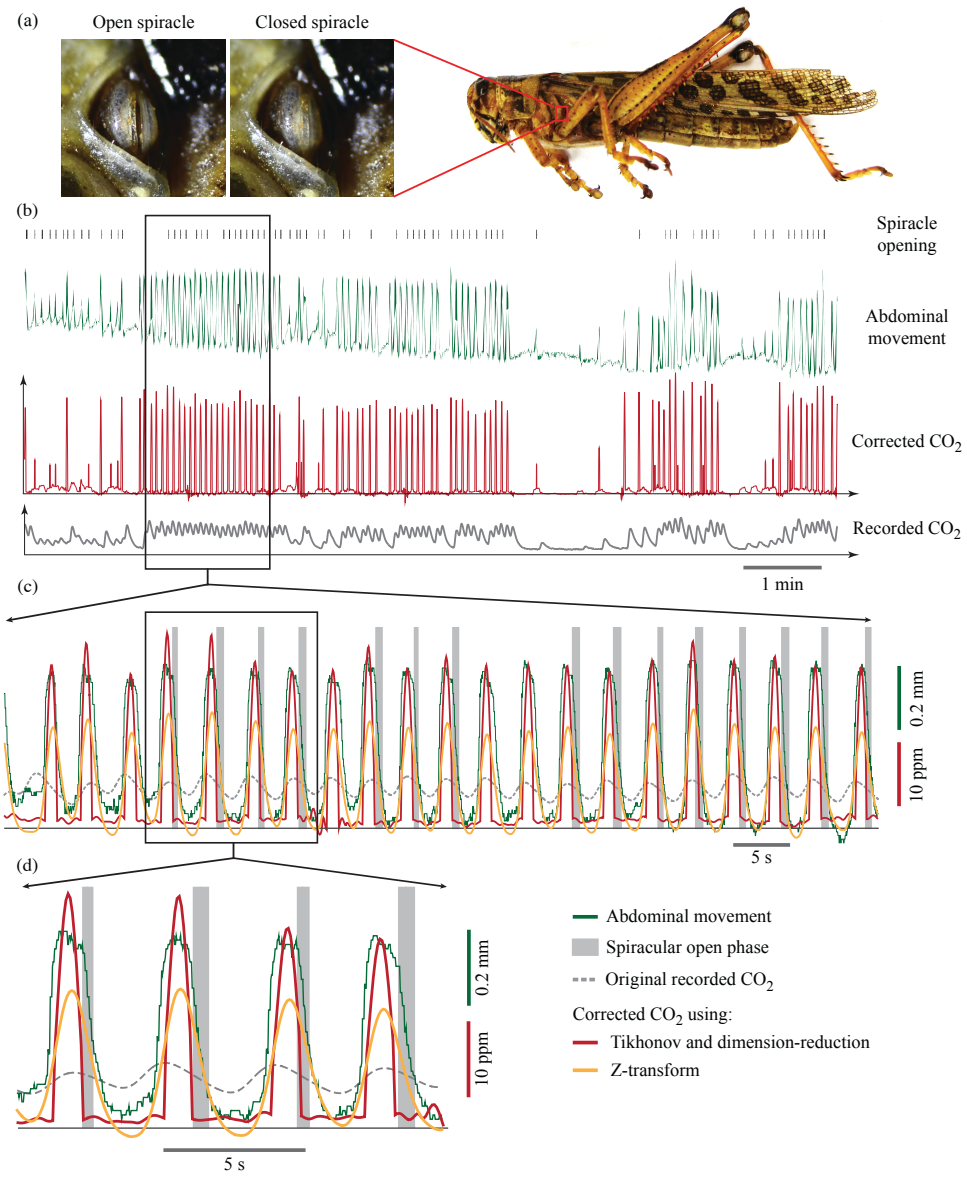

Figure 3.5: **Unidirectional airflow in grasshoppers.** (A) In this experiment, abdominal pumping, spiracular state, and CO_2 emission in a grasshopper were recorded and synchronized together. (B,C) The raw CO_2 signal shows a cyclic pattern of respiration. However, the corrected CO_2 signals shows discontinuous gas exchange, indicated by periods of CO_2 release. (D) The recovered CO_2 signal (corrected using the Tikhonov method) shows that abdominal pumping was concurrent with the CO_2 emission, but almost all the CO_2 burst happened when the thoracic spiracle was closed. The spiracles open when the abdomen starts to relax. The recovered CO_2 signal corrected using the Z-transform method did not reveal these details.

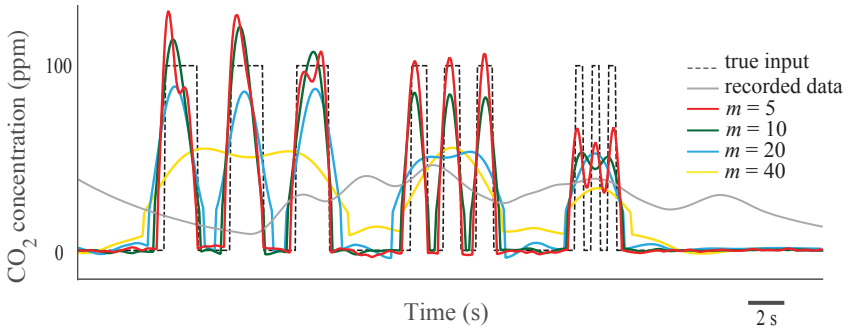

Figure 3.6: **The effect of the tuning factor (m) in the performance of recovery using DR method.** By choosing a small number for m in the dimension reduction method, the fast dynamical changes in the input signal can be recovered. However, the results can become noisy.

Chapter 4

Discussion

Here, we extended the well-known Tikhonov method for large-scale problems using a partitioning approach, and also presented a new dimension reduction method that reduces a large ill-conditioned problem to a set of smaller, better-conditioned problems. Both methods were tested computationally and experimentally on a flow-through respirometry system. Based on our computational and experimental evaluations, these methods exhibit nearly identical performance. Although the accuracy of both methods in recovering the true signal were similar, the dimension reduction method is computationally more efficient. In both methods, we compute the inverse matrix in (Equation (1.8) and Equation (2.5)), although for computational efficiency and stability, more sophisticated tools can be used.

In the Tikhonov method, we need to solve a system with coefficient matrix $\mathbf{H}^T\mathbf{H} + \gamma\mathbf{Q}^T\mathbf{Q}$. Although computing the inverse matrix $\mathbf{M}$ is the typical approach in many biological applications, this is not recommended, especially for large datasets, due to the fact that the process is computationally expensive and numerically unstable. A better approach is to compute a matrix factorization such as an LU or QR decomposition [10] of the coefficient matrix once, and then for each subsequent solve, use the computed matrix factorization to efficiently solve the system. For an $n \times n$ system, a general linear solve requires $O(n^3)$ floating-point operations [23], which could be a big number for large datasets. In addition, for problems where constructing the matrix is not desired, iterative methods are widely studied in the numerical linear algebra community for solving linear systems and linear least-squares problems.

Iterative approaches such as the Conjugate Gradient for Least Squares (CGLS) method or the LSQR method [13, 14] are typically fast in that they often produce good solutions in a few iterations. However, for the respirometry reconstruction problem, these methods require additional preconditioning to accelerate convergence. This is a topic of current research and is beyond the scope of this work. In respiratory problems the $\mathbf{H}$ matrix could be large. However, it is a spare matrix and it is constructed form the impulse response vector h, which has a much smaller size compared to the number of data points. In this research we showed that the inverse problem could be solved after calculating the inverse of a much smaller matrix $\mathbf{M}$, which is in the order of the length of h and not the number of data points.

In the dimension reduction method, a linear system including the matrix $\mathbf{L}^T\mathbf{H}^T\mathbf{HL}$ must be solved (Equation (2.5)), and its size is m times smaller than the size of the data that we consider at each cycle. The factor m will be different integers for different experimental setups. In our work, after experimentally tuning m, this number fell between 4 and 30 for different experiments and simulations with a variety of noise levels. Therefore, in these experiments and simulations, the size of the matrix was 4 to 30 times smaller, in comparison to that of the matrix for the modified, which can decrease the computational cost, particularly when the size of the impulse response (and consequently the size of the $\mathbf{H}$ matrix) is large.

Previously, it has been shown that the Tikhonov method exhibits much better performance in comparison with other methods such as trend identification, Kalman filtering, and Kalman smoothing [57]. However, applying the Tikhonov method requires calculating the inverse of a large matrix, with a size equal to the length of the data, or many iterations of a numerical optimization scheme. In contrast, the extension of the Tikhonov method and the dimension reduction methods that we provide in this study are applicable to large datasets of any size. The methods are reasonably straightforward and have only one parameter to be tuned. This feature makes them less complicated to use than the generalized Z-transform

(GZT) method, recently introduced by our group [50], which requires the use of multiple parameters that must be determined experimentally. Therefore, tuning of the Tikhonov method is simpler. Both of the new methods introduced here rely on a single parameter that should be tuned for best results: γ in the Tikhonov method, and m in the dimension reduction method. By increasing the tuning parameter, each method becomes less sensitive to noise in the data, but this comes at the cost of losing fidelity to the true input signal. In particular, these methods lose accuracy in estimating sharp changes of the input. Conversely, by decreasing the tuning parameter, the methods become better in capturing fast changes in the input, but this comes at the cost of becoming more sensitive to noise and errors (Figure 3.6). For standard Tikhonov regularization, many parameter-selection methods have been developed and investigated for automatically choosing the parameter; this includes the discrepancy principle and generalized cross-validation [15, 20, 58]. In practice, however, it is often desirable to tune the parameter via trial and error, based on the goals of the experiment. For instance, if determining fast changes in the input is crucial and some small amount of noise in the solution can be tolerated, a researcher can use a smaller γ in the Tikhonov method or m in the dimension reduction method. For the dimension reduction approach, we have not developed a method that can be used to determine the optimal value of m, and this remains a target for future study. In our simulations and experiments, we chose it by trial and error. One of the possible problems in the dimension reduction method is that the matrix $\mathbf{L}^T\mathbf{H}^T\mathbf{H}\mathbf{L}$ in Equation (2.5) becomes singular or nearly singular, making the inversion unstable. By the nature of their design, flow-through respirometry systems have a delay between the signal input and the measured output (τ in Figure 1.1) [42]. This phenomenon appears as n_0 zeroes at the beginning of the impulse response (h) and results in n_0 rows of zeroes in the matrix $\mathbf{H}$. This can cause a singularity in $\mathbf{H}^T\mathbf{H}$ and $\mathbf{L}^T\mathbf{H}^T\mathbf{H}\mathbf{L}$ in Equation (2.1) and Equation (2.7). In the Tikhonov method (Equation (1.8)), the regularization term $\gamma\mathbf{Q}^T\mathbf{Q}$ is able to deal with the singularity. For the dimension

reduction method (Equation (2.7)), we propose two methods to prevent singularity, even if the n_0 elements of the impulse response are forced to be zero:

1- We eliminate the delay and therefore the singularity by eliminating the n_0 zeros from the beginning of the impulse response, and eliminate the first n_0 data points from the output. After eliminating these points, the $\mathbf{H}$ matrix should be constructed based on the new impulse response, and the new output vector ($\mathbf{y}$) should be used in Equation (2.7). Applying this modification will not change the solution.

2- Similar to the Tikhonov method, we can add a regularization term ($\gamma\mathbf{Q}^T\mathbf{Q}$) to the projected problem. In this way, Equation (2.7) changes to $\mathbf{M} = \mathbf{L}(\mathbf{L}^T\mathbf{H}^T\mathbf{H}\mathbf{L} + \gamma\mathbf{Q}^T\mathbf{Q})^{-1}\mathbf{L}^T\mathbf{H}^T$.

The importance of the methods in physiological studies: In some studies, precisely determining the true timing of the gas exchange signal is crucial. In general, it becomes more important if we want to synchronize the gas exchange data with another fast dynamical event, such as a change in body temperature [6], body movement [47, 49], tracheal deformation [56], or even heartbeat [62]. To demonstrate the effectiveness of the methods on a real physiological system, we synchronized the CO_2 signal of a grasshopper with its abdominal and spiracular movements, both of which include relatively fast dynamics, with durations of the second or sub-second timescale. Therefore, the true CO_2 signal must be recovered with sub-second accuracy if we are to understand the relationship amongst the signals. Grasshoppers possess 10 pairs of spiracles, with two pairs on the thorax and eight pairs on the abdomen. The timing and pattern of spiracular opening and closing can vary wildly, depending on the metabolic needs of the animal [27, 28, 44]. Resting but alert grasshoppers normally exhibit abdominal pumping, driven by dorsoventral expiratory muscles [33]. If some of the spiracles are open, the contraction of the abdomen causes some parts of the tracheal system to compress [28], forcing the air out of the system. During exhalation, the first four posterior pairs of spiracles close, and expiration occurs through the last six pairs [33, 39]. When the abdomen relaxes,

spiracles 5-10 close and spiracles 1-4 open, and an increase in the volume of the tracheal system causes bulk flow of air into the body through the anterior spiracles [21, 44]. This spiracular timing during abdominal pumping helps to produce a unidirectional flow of air from anterior to posterior within the tracheal system [44]. A unidirectional flow of air is not unique to grasshoppers, and has been reported in beetles, bees, and cockroaches as well [5, 18, 29]. However, the determination of unidirectionality has been based on the observation of average air movement from the thorax to the abdomen side over a long period [5, 18, 21]. In these studies, an animal was put in a chamber with a barrier to separate the external air from the abdominal and thoracic sides. Over the course of minutes to hours, it is observed that the air gradually moves from the thorax to the abdomen side. Miller [44] also measured the abdominal movement and status of four spiracles simultaneously to infer the direction of flow. In his experiments, CO_2 was not measured, and expiration and inspiration were interpreted from the abdominal movement. However, we now know that abdominal pumping can be decoupled from respiration [25, 49], so this inference can be wrong. In our experiment, we simultaneously measured abdominal movement, spiracle movement, and CO_2 emission. The CO_2 signal recovery methods enabled the true respiratory signal to be discerned with sub-second resolution, which in turn enabled their synchronization with two other real-time signals. This helped us to directly observe, for the first time, the relationship between the true individual CO_2 expiration bursts, abdominal pumping, and the status of a spiracle in a grasshopper. Knowing the timing of the spiracles and how they coordinate with abdominal pumping, tracheal deformation, gas exchange, and other respiratory relevant signals is of fundamental importance to understanding the underlying mechanistic basis of active ventilation in insect respiration. However, measuring these events simultaneously can be difficult. Our data (Figure 3.5) show that when the grasshopper pumps its abdomen, it closes the thoracic spiracle and releases CO_2, which indicates that some of the other spiracles must be open within this duration. When the insect relaxes the abdomen, it opens the

thoracic spiracle, but there is almost no CO_2 emitted in this period, which suggests that the grasshopper is drawing the air in during this period. These observations are congruent with previous observations about active ventilation [25] and the unidirectionality of the airflow in grasshoppers [43, 60].

The Z-transform method, also known as the Bartholomew method, has perhaps been most widely used to correct gas exchange signals, but the temporal resolution of this method is not always sufficient to study fast changes in respiratory signals [50]. We compared the results of the grasshopper experiment using our new methods with those using the Z-transform method (Figure 3.5). As interpreted, the corrected CO_2 signal using the Z-transform method (Figure 3.5) would indicate the presence of CO_2 emission during all spiracular open phases, qualitatively different interpretation than what was obtained with our new methods. Using the Z-transform method, we would not have been able to clearly identify the evidence for unidirectional flow, demonstrating the power of the new methods. In any respirometry system, the washout problem reduces the accuracy of the recorded respiratory data, obscuring details of gas exchange. The issue becomes more problematic when we want to find the relationship between gas exchange and other fast dynamical events. Our demonstration with the grasshopper was only one example to show the importance of finding the true respiratory signal with fast dynamics, but the methods are broadly applicable for other types of respiratory studies. For example, they could be usefully applied in studies of the discontinuous gas exchange cycle (DGC), a topic of heavy debate [12, 42, 52, 53, 54]. DGC involves three phases: 1) the closed phase, in which the insect keeps the spiracles closed and consumes oxygen from the air sealed inside the tracheal system, with CO_2 buffered in the hemolymph; 2) the flutter phase, in which the spiracles open slightly and then close rapidly in sequence; and 3) the open phase, in which the insect keeps the spiracles open and releases CO_2. In many studies, the open phase is reported to last for several minutes to hours [12, 31]. But,

to the best of our knowledge, there is no explanation for the long duration of the open phase. The hygric [9], chthonic [40], and oxidative damage [31] hypotheses are the main proposed explanations for DGC, explaining that insects keep their spiracles closed for a long time to decrease water loss, to maximize the partial pressure gradient between the tracheal system and environment, or to keep the oxygen level down inside the tracheal system to minimize tissue damage, respectively. None of these hypotheses can explain why insects keep their spiracles open for a long time during the open phase. Keeping the spiracles open for a long duration can be detrimental for multiple reasons: it could lead to considerable water loss, decrease the partial pressure gradient, and/or expose the tissues to high levels of oxygen for a long time. However, our results from the grasshopper trial suggest that it might be possible that, during the so-called open phase, the spiracles are not actually open continuously. Instead, the spiracles may in fact close intermittently, but because of the washout issue and insufficient input estimation, the CO_2 signal wrongly indicates a continuous CO_2 emission, a point that has been previously suggested [24]. This behavior is congruent with discontinuous gas exchange of cockroaches, which have been observed to exhibit multiple opening and closing of spiracles in the open phase [35]. Based on our observations in this study, we also suggest that any interpretation from the raw CO_2 signal, or even the Z-transformed signal, could be misleading without using an accurate recovery method, such as the presented methods in this work.

4.1 Conclusions and Future Work

We have developed two new methods for accurately estimating the input signal in any physiological system. Our test case with a grasshopper demonstrates that these methods can be used to extract high temporal information for the original signal, which can dramatically

change the interpretation of the underlying physiological processes. Although the Tikhonov method is widely used for signal processing applications across fields, few researchers have employed it input estimation of physiological systems. The novelty of our modification of the Tikhonov method is that this extension makes it possible to apply the method to datasets of any size, including very large datasets. Furthermore, our new dimension reduction method can produce quality solutions that are similar to Tikhonov solutions, but in a slightly more efficient manner. This method has the potential to be beneficial in other applications such as image processing. To assist a researcher in implementing these methods for their own studies and to encourage further development of the methods, we have provided detailed instructions and the code as open source resources [48]. Overall, these improvements in input estimation have the potential to change the way physiologists view indirectly recorded data, most particularly for studies of gas exchange.

Appendices

Appendix A

Regularizing Properties of the Dimension Reduction Method

In this appendix, our goal is to provide justification and insight for the dimension reduction method. We first interpret the method as a projection approach, which is a form of regularization [26]. Let $\mathbf{H}$ be an $N \gg N$ convolution matrix of the form in Equation (1.5), and $\mathbf{L}$ be an $N \gg n$ matrix with entries given in Equation (2.3). By construction, columns of $\mathbf{L}$ are orthogonal, and a simple scaling by $1/\sqrt{m}$ makes them orthonormal. Because the columns of $\mathbf{L}$ form an orthonormal basis, the projected problem seeks an approximation to the solution that lies in a low-dimensional subspace of R^N. That is, Equation (2.1) constrains the solution to a low-dimensional subspace, which has a regularizing effect on the solution. Other common projection approaches are based on Krylov subspace methods [26]. The improved conditioning of the projected system, compared to the original system, can be explained by comparing matrices $\mathbf{H}$ and $\mathbf{HL}$. First, notice that columns of $\mathbf{HL}$ represent averages of neighboring columns in the Toeplitz matrix $\mathbf{H}$. Thus, if the columns of H are nearly linearly dependent, the columns of $\mathbf{HL}$ will be linearly independent. This is revealed in the rank of a matrix, which corresponds to the number of linearly independent columns. By properties of rank of a matrix, we have $\text{rank}(\mathbf{HL}) \leq \min(\text{rank}(\mathbf{H}), \text{rank}(\mathbf{L}))$

Typically, the rank of $\mathbf{H}$ is large (close to N) and $\mathbf{L}$ has full rank by construction, so we can assume that for sufficiently large m, $\mathbf{HL}$ is full rank (with rank n). A least-squares

problem with an overdetermined full rank system has a unique solution that satisfies the normal equations [4], which is used in our approach. In the context of inverse problems, the above interpretation of the dimension reduction method as a constraint on the solution makes sense in terms of regularization. It is worth noting that matrix $\mathbf{L}$ and its transpose strongly resemble prolongation and restriction operators used in the multigrid literature [8], but our approach is not a multigrid approach.

Appendix B

Deriving Equation (2.7) and Spectral Relationships

In Appendix B, we will derive Equation (2.7), and discuss spectral relationships among the reconstruction matrices. The dimension reduction method initially assumes that m consecutive inputs are equal, leading to the projected problem in Equation (2.1) and the computed solution in Equation (2.4). However, with this assumption, the solution cannot recover input changes during the intervals, so we improve the method by incrementally sliding the intervals m times and taking the final solution to be an average of the m solutions. Let $\mathbf{P}_k$ be a lower shift matrix whose $(i,j)^{th}$ component is: $(\mathbf{P}_k)_{ij} = \delta_{i,j+k-1}$, where δ is the Kronecker delta. For example, $\mathbf{P}_2\mathbf{x}$ shifts the components of vector $\mathbf{x}$ down by 1 element and introduces a zero in the first element, whereas $\mathbf{P}_2^T\mathbf{x}$ shifts the components of vector $\mathbf{x}$ up by 1 element and introduces a zero in the last element.

Thus to determine the k^{th} solution ($1 \leq k \leq m$), we first shift the output vector down by $k-1$ elements, which can be represented by matrix multiplication, $\mathbf{P}_k\mathbf{y}$. Here, we assume all outputs before time zero are zero ($y_j = 0$ if $j < k-1$). Then, we use the dimension reduction approach to compute a solution, $\mathbf{M}\mathbf{P}_k\mathbf{y}$. Finally, we shift the solution back up by $k-1$ elements, giving the k^{th} solution, $\mathbf{P}_k^T\mathbf{M}\mathbf{P}_k\mathbf{y}$.

Although this solution is not precise for last k entries of the input vector, we eliminate the last n_0 estimated inputs, so the lack of precision is inconsequential. Due to linearity

of matrix multiplication, the average of all estimations is given as $\hat{\mathbf{u}} = \tilde{\mathbf{M}}\mathbf{y}$, where $\tilde{\mathbf{M}} = \frac{1}{m}\sum_{k=1}^{m}\mathbf{P}_k^T\mathbf{M}\mathbf{P}_k$. Notice that since the $\mathbf{P}_k$ are shift matrices, $\mathbf{P}_k^T\mathbf{M}\mathbf{P}_k$ can be obtained by shifting rows of $\mathbf{M}$ up $k-1$ times and columns of $\mathbf{M}$ left $k-1$ times, and filling the remaining entries with zero. This is computationally easy to perform.

Appendix C

Recovering the true signal from a noisy data; simulation results

The Tikhonov method and Dimension Reduction method were computationally evaluated. In a simulation we used the methods to recover various rectangular input pulses with different frequencies. The frequency of the input signals are 0.1, 0.2, 0.5, 1 and 2 Hz. In order to examine the sensitivity of the methods on the data noise the simulation was repeated by adding 0.01%, 0.1%, 1%, 2%, 5%, and 10% normally-distributed noise to the output. We considered $n + n_0 = 1500$, at each iteration ($n_0 = 720$, Figure 1.1). The recovered inputs were compared with the true input at each frequency and each noise level separately. The regularization parameters γ and m for each experiment are reported in 3.1 and 3.2.

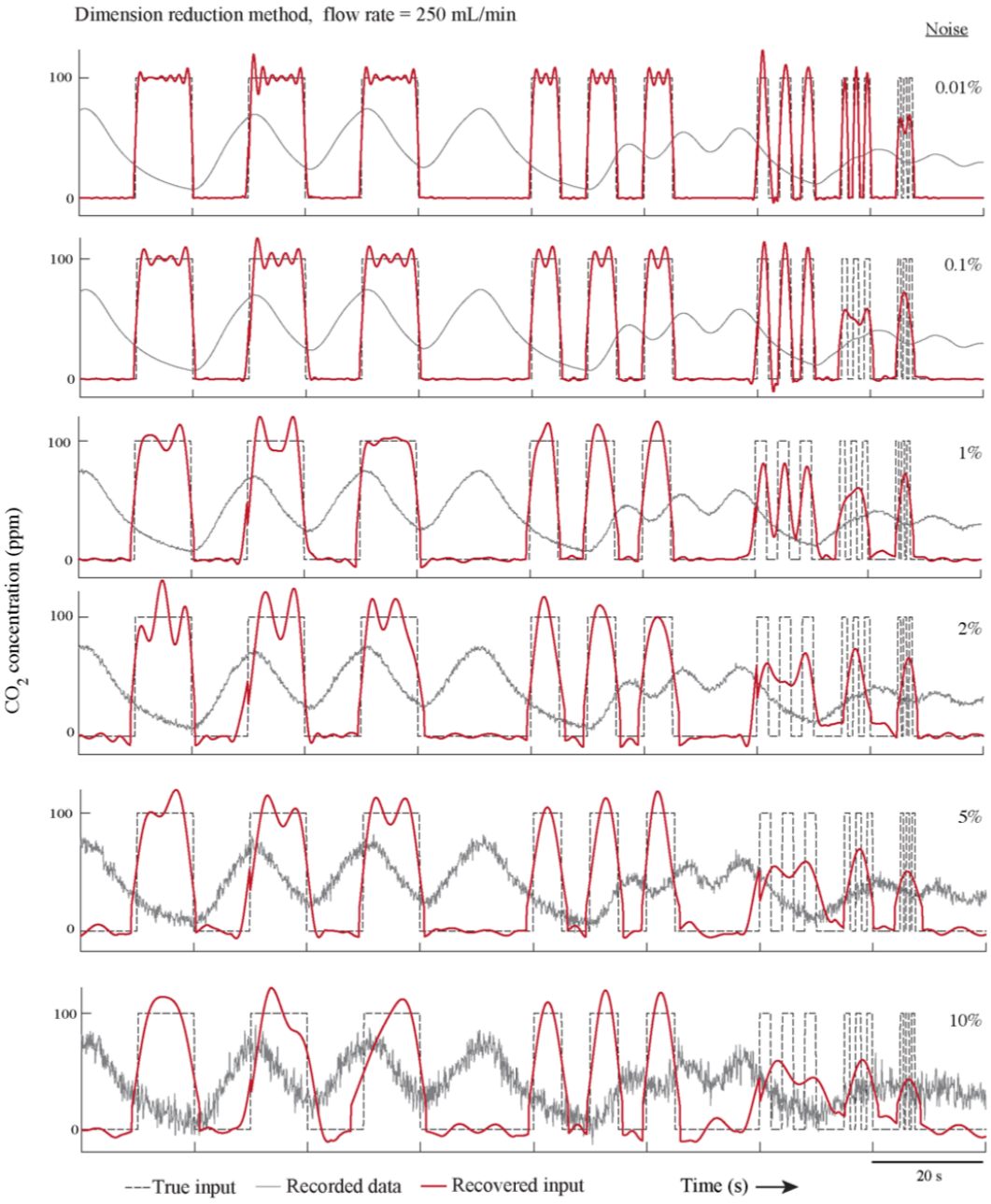
Dimension reduction method, flow rate = 250 mL/min
Noise
0.01%
0.1%
1%
2%
5%
10%
100
0
CO_2 concentration (ppm)
---True input
Recorded data
Recovered input
Time (s)
20 s

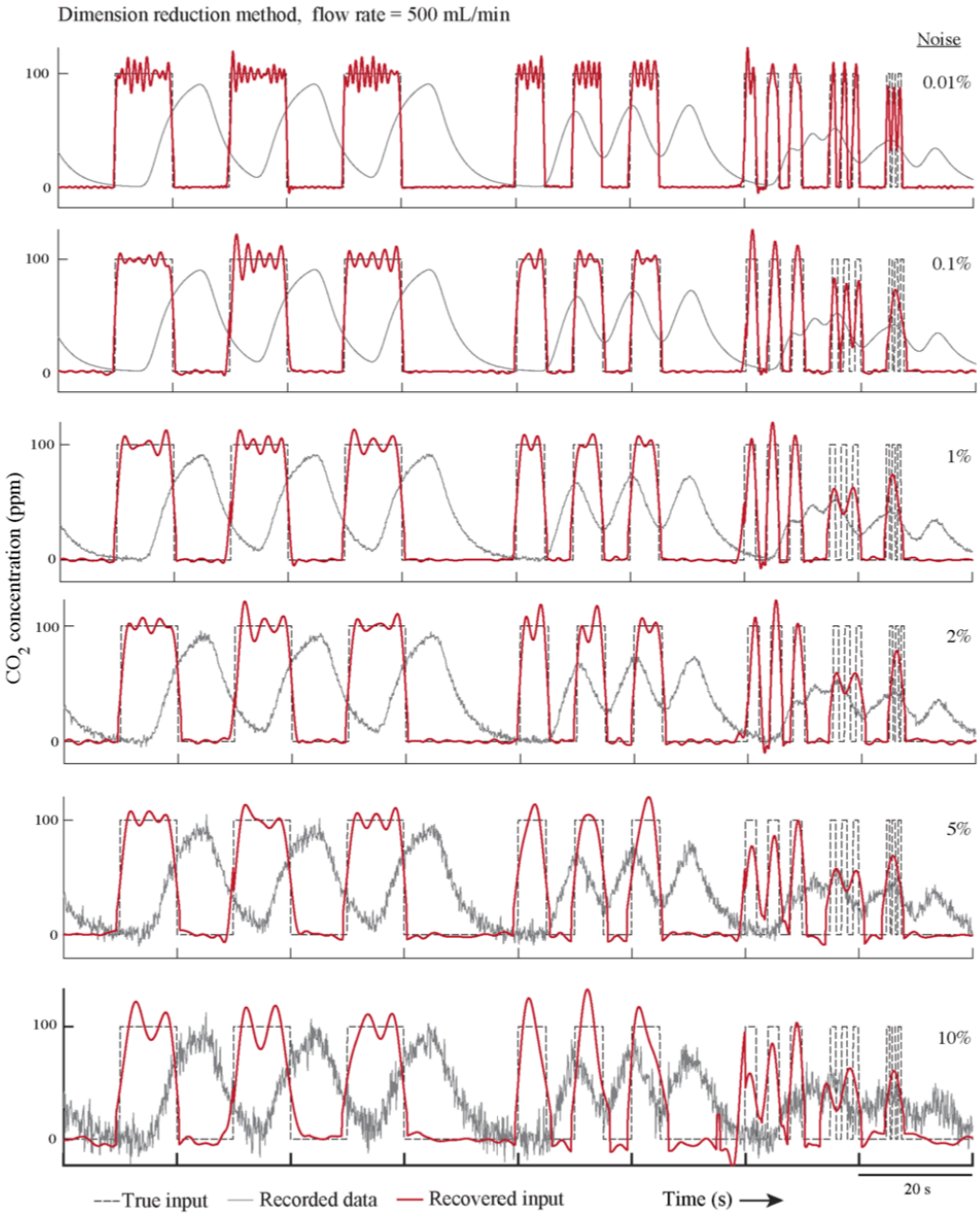
Dimension reduction method, flow rate = 500 mL/min
Noise
0.01%
0.1%
1%
2%
5%
10%
100
0
CO_2 concentration (ppm)
---True input
Recorded data
Recovered input
Time (s)
20 s

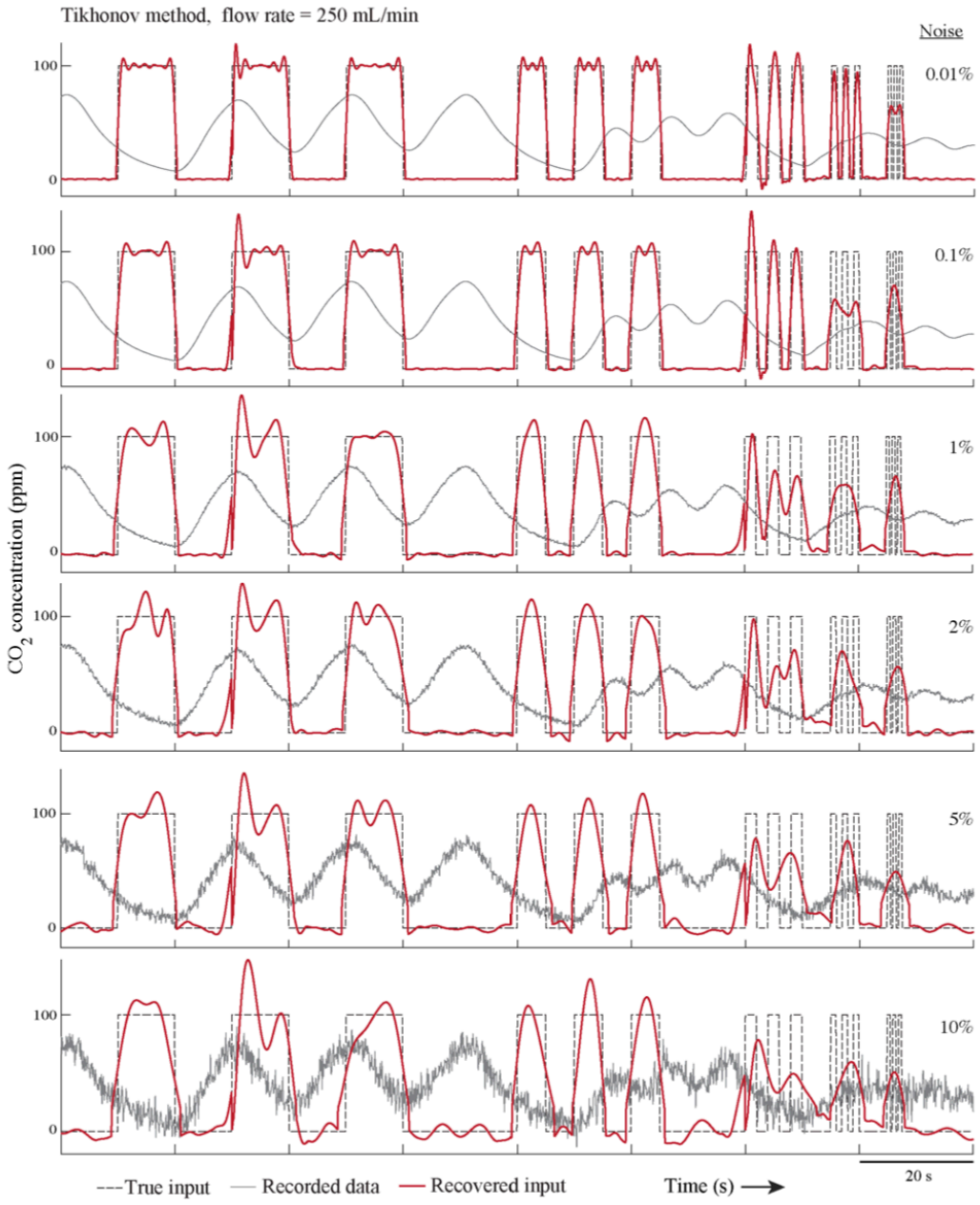
Tikhonov method, flow rate = 250 mL/min
Noise
0.01%
0.1%
1%
2%
5%
10%
100
0
CO_2 concentration (ppm)
---True input
Recorded data
Recovered input
Time (s)
20 s

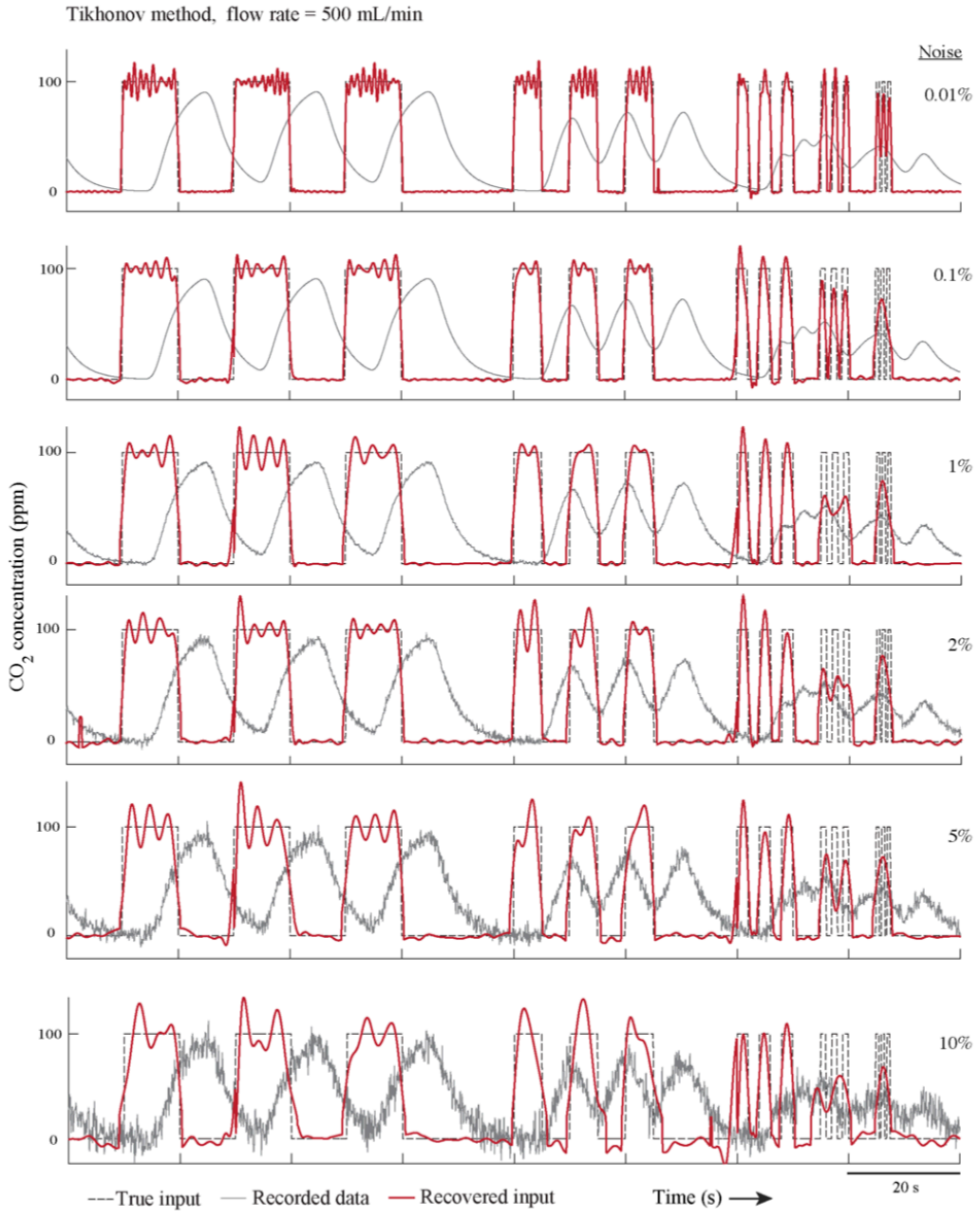
Tikhonov method, flow rate = 500 mL/min
Noise
0.01%
0.1%
1%
2%
5%
10%
100
0
CO_2 concentration (ppm)
---True input
Recorded data
Recovered input
Time (s)
20 s

Appendix D

Dynamics of flexible fins using vortex sheet

Understanding the principles of swimming and flying in animals can assist in developing underwater manoeuvres and micro-air vehicles. The fluid-structure interaction problem of flying and swimming is vastly studied by many scientists with the simplified models of a plate immersed in an inviscid fluid flow [1, 2, 11, 19, 34, 38, 63]. Since for most swimmers the fluid-fin mass ratio is large, fin mass is neglected in this model. The effect of wing and fin flexibility on the thrust magnitude and propulsive efficiency have been explored in many studies [2, 3, 38]. In this study we present a dynamical model for flexible fins with a negligible mass. In previous models the final equations are implicit, which makes them numerically inefficient. The presented model in this study provides an explicit set of equations.

D.1 Method

Here, we model the caudal fin of the fish as an inextensible elastic sheet in two dimensional incompressible inviscid flow with the length of $2L$. A prescribed motion is directly imparted to the leading edge of the fin in the form of an arbitrary pitch $\theta_0(t)$ and displacement $\xi_0(t)$ (Figure D.1). This could, for example, represent the motion of the rest of the fish body. The fin is considered a one dimensional Euler-Bernoulli beam with arbitrary and varying stiffness

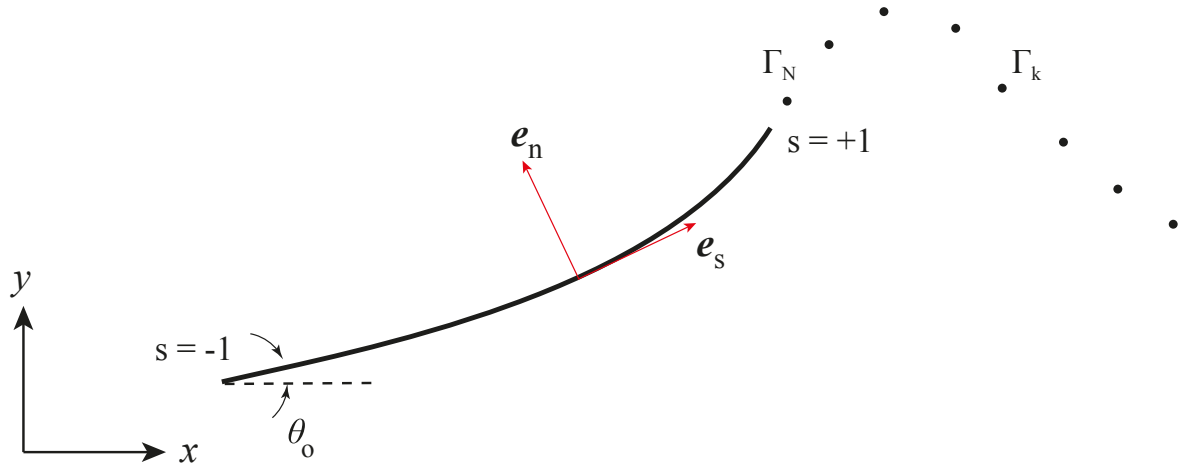

Figure D.1: **A schematic of the flexible fin.** The position and pitch angle θ_o of the leading edge $s = -1$ is assumed to be prescribed functions.

along its length. A pressure distribution is also considered along the length of the fin that is time varying due to the coupled fluid-structure interaction. Using thin airfoil theory, we identify the fin with a bound vortex sheet accounting for the infinitesimal attached boundary layers on either sides of it. The strength of the bound vortex sheet evolves with the movement of the fin. The free vortex sheet that develops in the wake is represented as a collection of discrete point vortices shedding from the trailing edge of the filament. Kelvin's theorem will be used to ensure that the circulation in the fluid domain remains constant and use this phenomenon to determine the intensity of the latest released vortex element. According the the Helmholtz laws the strength of each free vortex element remains constant after being released from the trailing edge. Modeling the fin with a bound vortex sheet and the wake behind it with free vortex elements let us determine the flow field using the Biot-Savart law as the superposition of contributions from all vortex elements and the vortex sheet.

The caudal fin in most fish has negligible mass compared to the rest of the body. Furthermore, as shown in the results of this study, hydrodynamical forces dominate the dynamics

of the fin. Therefore, we neglect the mass of the fin in our model. This assumption leads to an important simplification in the model, which makes it computationally efficient. We also assume that there is no vortex shedding from the leading edge, since the leading edge is connected to the streamlined fish body and the angle of attack usually remains small.

In this model, five main unknown parameters are: 1) the shape of the fin, 2) strength of the bound vortex-sheet, 3) the pressure distribution on the fin, 4-5) strength and location of the free vortex elements. In the following sections, sets of equations are derived to find these unknowns. In short, these sets of equations are the outcomes of Newton's Second Law, boundary condition of the fin, the unsteady Bernoulli equation, no penetration boundary condition, Kelvin's circulation theorem, and the Biot-Savart law. We set up a series of explicit and linear equations to find the shape evolution and vortex strength evolution of the fin and the location of the free vortex elements.

D.1.1 Dynamics of the fin

The dynamic model of the massless fin is governed by Euler-Bernoulli beam theory, and can be represented using Newton's Second Law as:

$$\frac{\partial}{\partial s}(T\hat{e}_s) - R\frac{\partial}{\partial s}(\frac{\partial}{\partial s}(\kappa B)\hat{e}_n) - [p]\,\hat{e}_n = 0, \tag{D.1}$$

where T is the tension force, $[p]$ is the pressure jump across the fin, κ is the curvature, and B is the nondimensionalized rigidity of the beam, which could vary along the beam. s is arclength ($-1 \leqslant s \leqslant 1$) that is used as a Lagrangian coordinate in the equations. $\hat{e}_s$ and $\hat{e}_n$ are the tangential and normal unit vectors at s. The constant $R = \frac{B_o}{\rho_f L^5 \left(\frac{\omega}{2\pi}\right)^2}$ is the dimensionless rigidity of the fin, where B_o is the rigidity of the fin near the leading-edge. Here, L is used as the length scale, $2\pi/\omega$ as the time scale , and $\rho_f L^3 \left(\frac{\omega}{2\pi}\right)^2$ as the force scale

to nondimensionalize the equations.

The location of any point on the beam can be written using complex variables as $\xi(s,t) = x(s,t) + iy(s,t)$. The tangential and normal unit vectors can be determined from the fin shape as: $\hat{e}_s = \xi_s = e^{i\theta(s,t)}$ and $\hat{e}_n = ie^{i\theta(s,t)}$ respectively, where $\theta(s,t) = \tan^{-1}(\frac{y_s(s,t)}{x_s(s,t)})$ is the local tangent angle at any point $\xi(s,t)$. The curvature at any point depends on the fin shape as $\kappa(s,t) = \theta_s(s,t)$.

The boundary conditions at the free trailing-edge ($s = 1$) are given by prescribed functions:

$$T = \kappa = \kappa_s = 0 \tag{D.2}$$

and the position and orientation of the leading-edge ($s = -1$) that is driven by the fish body are given by :

$$\theta|_{s=-1} = \theta_0(t); \quad \xi|_{s=-1} = \xi_0(t). \tag{D.3}$$

Integrating the tangential component of equation (D.1) from the trailing edge to any arbitrary point on the fin yields the tension force:

$$T = R\int_s^1 \kappa(\kappa B)' ds', \tag{D.4}$$

which satisfies the boundary condition (D.2). The normal component of equation (D.1) yields the pressure jump across the fin in terms of the tension force:

$$[p] = \kappa T - R(\kappa B)''. \tag{D.5}$$

There is no pressure jump across the free vortex sheet. Therefore, to impose the unsteady

Kutta condition while ensuring the continuity of the fluid pressure on either side of the vortex sheet, the pressure jump has to vanish at the trailing-edge; i.e. $[p]\,|_{s=1} = 0$, which is implemented in equation (D.5).

Equation (D.5) shows that the pressure distribution on the fin is a function of the shape, which is a consequence of neglecting the fin mass. Inclusion of fin mass in the model couples the fin accelerations with the pressure distribution (see [2] for example). This coupling leads to implicit solutions that are computationally expensive and require the iterative solution of a linear system at each time step. In cases where inertia is not very important to the physics of the problem, e.g., when the density of the filament is significantly less than the density of the surrounding fluid, we can incorporate the 'negligible-mass' model to obtain an explicit solution.

D.1.2 Evolution of the fin shape

To satisfy the no-penetration boundary condition on the fin surface, the fluid velocity must be equal to the fin velocity in the normal direction. To impose this condition we need to find the fluid velocity near the fin. The Biot–Savart equation provides the complex conjugate of fluid velocity at any arbitrary point, except on the vortex sheet, in terms of the attached vortex strength and free vortex elements;

$$\bar{w} = u_x - iu_y = u_o + \frac{1}{2\pi i}\int_{-1}^{1} \frac{\gamma(s',t)}{z-\xi(s',t)}ds' + \frac{1}{2\pi i}\sum_{k=1}^{N}\frac{\Gamma_k}{z-z_k(t)}, \tag{D.6}$$

where u_x and u_y are the velocity components of the fluid, $\gamma(s,t)$ is the vortex strength at point s on the fin, $\xi(s,t)$ is the shape function of the fin, and z_k and Γ_k are the location and the strength of the k^{th} free vortex element, assuming there are N free vortex elements in the fluid at the moment. The average flow velocity near any point on the vortex sheet can be

found by replacing z with $\xi(s,t)$:

$$\bar{w} = u_o + \frac{1}{2\pi i} \fint_{-1}^{1} \frac{\gamma(s',t)}{\xi(s,t) - \xi(s',t)} ds' + \frac{1}{2\pi i} \sum_{k=1}^{N} \frac{\Gamma_k}{\xi(s,t) - z_k(t)}. \tag{D.7}$$

Equation (D.7) provides the average fluid velocity on either side of the fin. It is known that the bound vortex sheet strength $\gamma(s,t)$ has an inverse-square-root singularity near both the leading and trailing edges [45], and can be replaced by $\frac{\nu(s,t)}{\sqrt{1-s^2}}$, where ν is the bounded part of γ.

$$\bar{w} = u_o + \frac{1}{2\pi i} \fint_{-1}^{1} \frac{\nu(s',t)}{\sqrt{1-s'^2}(\xi(s,t) - \xi(s',t))} ds' + \frac{1}{2\pi i} \sum_{k=1}^{N} \frac{\Gamma_k}{\xi - z_k}. \tag{D.8}$$

The position of the points on the fin can be written as $\xi(s,t) = \xi_0 + \int_{-1}^{s} \hat{e}_s(s',t) ds'$, where ξ_0 is the prescribed position of the leading-edge. Taking a derivative of this equation yields the velocity of the points on the fin as:

$$\dot{\xi} = \dot{\xi}_0 + \int_{-1}^{s} \dot{\theta} \hat{e}_n ds'. \tag{D.9}$$

Fluid cannot penetrate into the fin. Therefore the normal component of the fluid velocity adjacent to the fin must be equal to the normal component of the fin velocity:

$$\dot{\xi} \cdot \hat{e}_n = w \cdot \hat{e}_n. \tag{D.10}$$

It is well known that in the vortex sheet method it is not possible to satisfy the no-penetration constraint on all points of the fin, and it can only be satisfied in a limited number of points. Therefore, the constraint equation (D.10) will be imposed on n collocation points, such as $s_1, s_2, .., s_n$.

D.1.3 Vortex evolution

The unsteady Bernoulli equation shows that the strength of the fin vortex sheet evolves as:

$$\dot{\gamma} + \frac{\partial}{\partial s}\left(v_{rel}\gamma\right) = \frac{\partial}{\partial s}\left[p\right], \tag{D.11}$$

where v_{rel} is the relative velocity between the fluid and fin in the tangential direction $v_{rel}(s,t) = (w(s,t) - \dot{\xi}(s,t))\cdot \hat{e}_s$. In this equation the unknowns are the evolution rate of the beam shape $\dot{\xi}$, and the evolution rate of the bound vortex strength $\dot{\gamma}$. Meanwhile, the pressure jump is a function of the fin shape (D.5). After determining the pressure jump from (D.5) we substitute it here in equation (D.11). The unsteady Bernoulli equation can be used in the format of (D.11), or the integral of equation (D.11):

$$\int_1^s \dot{\gamma}(s',t)ds' = [p] - v_{rel}\gamma + v_{rel}\gamma|_{s=1}, \tag{D.12}$$

in which the right side is known and $\dot{\gamma}$ and v_{rel} on the left side are unknown. The integral form of the unsteady Bernoulli equation looks to be more complicated than the differential form (D.11). However, as we show in the numerical method section, the integral of $\dot{\gamma}$ has a simple form, and the singularity in $\dot{\gamma}$ can be eliminated.

D.2 Numerical Method

Equations (D.10)-(D.12) are nonlinear coupled singular integro-differential equations. Previously, implicit numerical methods have been developed to solve the equations of a flexible fin [2, 19, 55]. Here we show that for fins of negligible mass, it is possible to obtain an explicit numerical solution. The negligible mass assumption helps to find a closed form solution for

the pressure distribution equation (D.5). Therefore, knowing the shape of the fin at each time step, the value of the pressure is known, which is not the case in previous models that include the fin mass. Taking into account the fin mass in the model couples the pressure distribution and fin body acceleration. Thus, the pressure distribution and the fin body accelerations in Newton's equation, and the fin velocity $\dot{\xi}$ and vortex sheet strength γ in the unsteady-Bernoulli equation (D.12) all must be determined simultaneously. This complication leads to implicit solutions, which are inherently computationally expensive and require the solution of a nonlinear system at each time step.

The pressure jump $[p]$ is a function of the fin shape equations (D.3). Therefore it will be known at each time step of the numerical solution. The remaining unknowns are the rate of change of the fin shape $\dot{\xi}(s,t)$, and evolution of the vortex strength $\dot{\gamma}(s,t)$, strength of the newly released vortex element Γ_{N+1}, and velocity of the free vortex elements $\dot{z}_k$. After determining $\dot{\xi}$, $\dot{\gamma}$, and $\dot{z}_k$, they will be integrated over time to find the fin shape, attached vortex strength, and the new location of the free vortex elements. Consequently, the fluid velocity field and pressure distribution in the next time step will be determined. In order to find these functions we consider their Chebyshev expansion, and substitute them in the equations to find the coefficients of the expansion as:

$$\gamma(s,t) = \frac{\nu(s,t)}{\sqrt{1-s^2}} = \frac{1}{\sqrt{1-s^2}} \sum_{k=0}^{m_1} a_k(t) T_k(s), \tag{D.13}$$

$$\theta(s,t) = \theta_o(t) + \sum_{k=0}^{m_2} b_k(t) T_k(s), \tag{D.14}$$

where $T_k(s)$ is the k^{th} Chebyshev polynomial of the first kind. The expansion of γ and θ equations (D.13) – (D.14) should satisfy the trailing edge boundary condition (D.2), leading-edge boundary condition (D.3), no-penetration condition (D.10), and the unsteady-

Bernoulli equation (D.12). The boundary conditions at the leading and trailing edges are $\kappa|_{s=1} = \theta_s|_{s=1} = 0$, $\kappa_s|_{s=1} = \theta_{ss}|_{s=1} = 0$, and $\theta|_{s=-1} = \theta_o$. By substitution of the polynomial form of θ from (D.14) into these boundary conditions, we obtain the following constraints on b_k's:

$$\sum_{k=0}^{m_2} k^2 b_k(t) = 0, \tag{D.15}$$

$$\sum_{k=0}^{m_2} \frac{1}{3} k^2(k^2-1) b_k(t) = 0, \tag{D.16}$$

$$\sum_{k=0}^{m_2} (-1)^k b_k(t) = 0. \tag{D.17}$$

Before substituting the expansions of γ and θ in the no penetration condition, equation (D.10), we eliminate the integrals from this equation. We can separate the singular part inside the integral in equation (D.7) using Taylor expansion [2]:

$$\frac{1}{\xi(s,t) - \xi(s',t)} = \frac{1}{\xi_s(s-s')} + K(s,s'), \tag{D.18}$$

where $K(s,s')$ is the smooth part and can be found numerically at each iteration from the above equation if $s \neq s'$. Using $\xi_s = e^{\theta}$ and $\theta_s = \kappa$, we can show that $K|_{s=s'} = \frac{i\kappa(s)}{2\xi_s} = \frac{-\xi_{ss}}{2\xi^2}$, which will be numerically calculated at each point. We then substitute ν and θ from equations (D.13) and (D.14) in the singular integral in equation (D.7):

$$\frac{1}{2\pi i} \fint_{-1}^{1} \frac{\nu(s',t)}{\sqrt{1-s'^2}(\xi(s,t) - \xi(s',t))} ds' = \frac{1}{2\pi i \xi_s} \int_{-1}^{1} \frac{\sum_{k=0}^{m_2} a_k T_k(s')}{\sqrt{1-s'^2}(s-s')} ds' + \frac{1}{2\pi i} \int_{-1}^{1} \frac{\nu(s',t) K(s,s',t)}{\sqrt{1-s'^2}} ds'. \tag{D.19}$$

The first integral on the right hand side can be determined in terms of the Chebyshev polynomials of the second kind and the second integral can be determined numerically using change of variable $s = cos\phi$:

$$\frac{1}{2\pi i}\fint_{-1}^{1}\frac{\nu(s',t)}{\sqrt{1-s'^2}(\xi(s,t)-\xi(s',t))}ds' = \frac{i}{2\xi_s}\sum_{k=1}^{m_1}a_k U_{k-1}(s)+ \frac{1}{2\pi i}\int_0^{\pi}\nu(\phi',t)K(\phi,\phi',t)d\phi', \quad \text{(D.20)}$$

where $U_k(s)$ is the k^{th} Chebyshev polynomial of the second kind. The right hand side of this equation does not contain any singularities and the integral part can be easily computed numerically. Therefore the conjugate average fluid velocity at the fin can be written as:

$$\bar{w} = u_o + \frac{i}{2\xi_s}\sum_{k=1}^{m_1}a_k U_{k-1}(s) + \frac{1}{2\pi i}\int_0^{\pi}\nu(\phi',t)K(\phi,\phi',t)d\phi' + \frac{1}{2\pi i}\sum_{k=1}^{N}\frac{\Gamma_k}{\xi(s,t)-z_k(t)}. \quad \text{(D.21)}$$

At each time iteration w can be found from the above equation and be replaced on the right side of the no-penetration constraint equation (D.10).

The normal and tangential components of $\dot{\xi}$ show up in the no-penetration and unsteady-Bernoulli equations respectively and they contain $\dot{b}_k$ coefficients, which are unknown. To simplify these equations, we split $\dot{\xi}$ into tangential and normal components:

$$\dot{\xi} = (\tau_0^s + \sum_{k=0}^{m_2}\dot{b}_k\sigma_k^s)\hat{e}_s + (\tau_0^n + \sum_{k=0}^{m_2}\dot{b}_k\sigma_k^n)\hat{e}_n, \quad \text{(D.22)}$$

where

$$\tau_0^{s/n}(s) = \hat{e}_{s/n}\cdot(\dot{\xi}_o + \dot{\theta}_o\int_{-1}^{s}\hat{e}_n(s')ds'), \quad \text{(D.23)}$$

$$\sigma_k^{s/n}(s) = \hat{e}_{s/n}\cdot\int_{-1}^{s}T_k(s')\hat{e}_n(s')ds', \quad \text{(D.24)}$$

which can be calculated numerically at each iteration. By substitution of w from equation (D.21) and $\dot{\xi}$ from equations (D.22)-(D.24), the no penetration constraint, equation (D.10), can be written as:

$$\sum_{k=0}^{m_2} \sigma_k^n \dot{b}_k = w \cdot \hat{e}_n - \tau_o^n, \tag{D.25}$$

which must be satisfied in all the n collocation points $(s_1, s_2, ..s_n)$. Because equation (D.21) provides $\bar{w}$ instead of w, to calculate the right hand side of equation (D.25) we use $w \cdot \hat{e}_n = Re\{\bar{w}\hat{e}_n\}$. By combining equations (D.25) and (D.15)-(D.17), we obtain a system of linear equations that gives us $\dot{b}_k$'s. To match the number of unknowns and equations m_2 must be equal to $n+2$. Lastly, we substitute the Chebyshev expansions of θ and γ in the Bernoulli equation (D.12) to construct a system of equations to find $\dot{a}_k$'s. The integral on the left hand side of equation (D.12) can be simplified as

$$\int_1^s \dot{\gamma}(s',t)ds' = \sum_{k=0}^{m_1} \int_1^s \frac{T_k(s')ds'}{\sqrt{1-s'^2}} = \sum_{k=0}^{m_1} \delta_k(s)\dot{a}_k, \tag{D.26}$$

where using the change of variable $s = \cos\phi$ in the integral $\delta_k(s) = \int_{-1}^{s} \frac{T_k(s')}{\sqrt{1-s'^2}} ds' = \int_{\pi}^{\cos^{-1}(s)} -\cos(k\phi)d\phi$, which yields:

$$\delta_k(s) = \begin{cases} \pi - \cos^{-1}(s), & k = 0; \\ \dfrac{-1}{k}\sin(k\ \cos^{-1}(s)), & k \geqslant 1. \end{cases} \tag{D.27}$$

The relative velocity v_{rel} in the Bernoulli equation (D.12) is the difference between tangential velocities of the fluid and fin:

$$v_{rel} = (w - \dot{\xi}) \cdot \hat{e}_s = w \cdot \hat{e}_s - (\tau_0^s + \sum_{k=0}^{m_2} \dot{b}_k \sigma_k^s). \tag{D.28}$$

Because $\dot{b}_k$'s are determined in the previous step, v_{rel} can be computed here and substituting

it in the Bernoulli equation results in a system of linear equations for $\dot{a}_k$'s:

$$\sum_{k=0}^{m_1} \delta_k(s)\dot{a}_k = [p] - v_{rel}\gamma + v_{rel}\gamma|_{s=1}. \tag{D.29}$$

This equation should be satisfied in m_1+1 points (number of a_k's). For simplicity, we assume $m_1 = n-1$ and use the same collocation points as in equation (D.25). The quantities $\dot{a}$ and $\dot{b}$ can be found from equations (D.15)-(D.17), (D.25) and (D.29) and then integrated over time to find a and b's for the next time step.

To satisfy Kelvin's Theorem, conservation of circulation in the flow, at each time step a new vortex element will be shed from the trailing edge. Here we assume the total circulation in the fluid is zero at the beginning of the simulation. Therefore the strength of the newly shed vortex is:

$$\Gamma_{N+1} = -\int_{-1}^{1} \gamma(s)ds - \sum_{k=1}^{N} \Gamma_k. \tag{D.30}$$

The position of the newly shed vortex element (Γ_{N+1}) is assumed to be at the trailing edge. The location of the free vortex elements is updated by calculating the velocity of them using the Birkhoff–Rott equation:

$$\dot{\bar{z}}_j = u_o + \frac{1}{2\pi i}\int_{-1}^{1} \frac{\nu(s',t)}{\sqrt{1-s'^2}(z_j - \xi(s',t))}ds' + \frac{1}{2\pi i}\sum_{k=1,k\neq j}^{N+1} \frac{\Gamma_k}{z_j - z_k}. \tag{D.31}$$

After finding the velocity of the free vortex elements, we integrate them to update their location. Since the location of the newly released vortex is the trailing edge, the integral in the equation (D.31) becomes singular. To solve this problem we add a small desingularization parameter δ [36, 37] in the integral part:

$$\dot{\bar{z}}_j = u_o + \frac{1}{2\pi i}\int_{-1}^{1} \frac{\nu(s',t)(z_j - \xi(s',t))}{\sqrt{1-s'^2}[(z_j - \xi(s',t))^2 + \delta^2]}ds' + \frac{1}{2\pi i}\sum_{k=1,k\neq j}^{N+1} \frac{\Gamma_k}{z_j - z_k}, \tag{D.32}$$

or

$$\dot{\bar{z}}_j = u_o + \frac{1}{2\pi i}\int_0^{\pi} \frac{\nu(\phi',t)(z_j - \xi(\phi',t))d\phi'}{(z_j - \xi(\phi',t))^2 + \delta^2} + \frac{1}{2\pi i}\sum_{k=1,k\neq j}^{N+1} \frac{\Gamma_k}{z_j - z_k}. \tag{D.33}$$

The core objective in computationally simulating the fin is to find the $\dot{a}$ and $\dot{b}$ at each time and integrate them to update the shape of the fin ξ and the bound vortex strength $\gamma(s,t)$. The rest of the unknowns, i.e., pressure jump distribution, thrust, and flow velocity field, are functions of ξ and γ. We summarize this procedure in the following numerical algorithm:

step 0: Find $\delta_k(s)$ from equation (D.27) for $s = s_1, \ldots, s_n$ and $k = 1, \ldots, m_1$. The value of $\delta_k(s)$ depends only on s. Therefore, these values remains constant.

step 1: Update a and b coefficients in equations (D.13) and (D.14) to find $\nu(s,t)$ and $\theta(s,t)$ at the current time step. The unit vectors $\hat{e}_n$ and $\hat{e}_s$, the shape of the fin ξ, curvature κ, $\tau_0^{s/n}(s)$ and $\sigma_k^{s/n}(s)$ in equations (D.23) and (D.24) can be found using the updated θ.

step 2: Find the tension using equation (D.4) and substitute it in equation (D.5) to find the pressure jump distribution, $[p](s,t)$.

step 3: Use equation (D.18) to find the value of $K(s,s')$ for any $(s,s') = (s_j, s_k)$, when $1 \leq j,k \leq n$ (combination of collocation point).

step 4: Find the velocity of fluid at the collocation points using equation (D.21).

step 5: Find $\dot{b}_k$'s from equations (D.15)-(D.17) and (D.25).

step 6: Find the velocity of the fin from equation (D.22) and v_{rel} from equation (D.28).

step 7: Find $\dot{a}_k$'s from equation (D.29).

step 8: Integrate $\dot{a}_k$ and $\dot{b}_k$'s to update a_k and b_k's.

step 9: Find the strength of the newly released vortex element using Kelvin's Theorem, equation (D.30).

step 10: Find the velocity of the free vortex elements using equation (D.31) and (D.33), then integrate them to update the position of them.

step 11: Replace N with $N + 1$ and then go back to step 1.

Bibliography

[1] Silas Alben. An implicit method for coupled flow–body dynamics. *Journal of Computational Physics*, 227(10):4912–4933, 2008.

[2] Silas Alben. Simulating the dynamics of flexible bodies and vortex sheets. *Journal of Computational Physics*, 228(7):2587–2603, 2009.

[3] Silas Alben and Michael J Shelley. Flapping states of a flag in an inviscid fluid: bistability and the transition to chaos. *Physical review letters*, 100(7):074301, 2008.

[4] Uri M Ascher and Chen Greif. *A First Course on Numerical Methods*. SIAM, 2011.

[5] L Bailey. The respiratory currents in the tracheal system of the adult honey-bee. *Journal of Experimental Biology*, 31(4):589–593, 1954.

[6] George A Bartholomew and M Christopher Barnhart. Tracheal gases, respiratory gas exchange, body temperature and flight in some tropical cicadas. *Journal of Experimental Biology*, 111(1):131–144, 1984.

[7] George A Bartholomew, David Vleck, and Carol M Vleck. Instantaneous measurements of oxygen consumption during pre-flight warm-up and post-flight cooling in sphingid and saturniid moths. *Journal of Experimental Biology*, 90(1):17–32, 1981.

[8] William L Briggs, Van Emden Henson, and Steve F McCormick. *A Multigrid Tutorial*. SIAM, 2000.

[9] John Buck, Margaret Keister, and H Specht. Discontinuous respiration in diapausing agapema pupae. In *Anatomical record*, volume 117, pages 541–541. Anat Rec, 1953.

[10] James R Bunch and John E Hopcroft. Triangular factorization and inversion by fast matrix multiplication. *Mathematics of Computation*, 28(125):231–236, 1974.

[11] Stephen Childress, Nicolas Vandenberghe, and Jun Zhang. Hovering of a passive body in an oscillating airflow. *Physics of Fluids*, 18(11):117103, 2006.

[12] Steven L Chown, Allen G Gibbs, Stefan K Hetz, C Jaco Klok, John RB Lighton, and Elrike Marais. Discontinuous gas exchange in insects: a clarification of hypotheses and approaches. *Physiological and Biochemical Zoology*, 79(2):333–343, 2006.

[13] Julianne Chung, Sarah Knepper, and James G Nagy. Large-scale inverse problems in imaging. *Handbook of Mathematical Methods in Imaging*, 1, 2015.

[14] Julianne Chung and James G Nagy. An efficient iterative approach for large-scale separable nonlinear inverse problems. *SIAM Journal on Scientific Computing*, 31(6):4654–4674, 2010.

[15] David Colton, Michele Piana, and Roland Potthast. A simple method using morozov's discrepancy principle for solving inverse scattering problems. *Inverse Problems*, 13(6):1477, 1997.

[16] Giuseppe De Nicolao, Diego Liberati, and Alessandro Sartorio. Deconvolution of infrequently sampled data for the estimation of growth hormone secretion. *IEEE Transactions on Biomedical Engineering*, 42(7):678–687, 1995.

[17] Giuseppe De Nicolao, Giovanni Sparacino, and Claudio Cobelli. Nonparametric input estimation in physiological systems: problems, methods, and case studies. *Automatica*, 33(5):851–870, 1997.

[18] Frances D Duncan and Marcus J Byrne. Respiratory airflow in a wingless dung beetle. *Journal of Experimental Biology*, 205(16):2489–2497, 2002.

[19] Jeff D Eldredge and David Pisani. Passive locomotion of a simple articulated fish-like system in the wake of an obstacle. *Journal of Fluid Mechanics*, 607:279–288, 2008.

[20] Heinz Werner Engl, Martin Hanke, and Andreas Neubauer. *Regularization of inverse problems*, volume 375. Springer Science & Business Media, 1996.

[21] Gottfried Fraenkel. Untersuchungen über die koordination von reflexen und automatisch-nervösen rhythmen bei insekten. *Zeitschrift für vergleichende Physiologie*, 16(2):418–443, 1932.

[22] Gene H Golub, Per Christian Hansen, and Dianne P O'Leary. Tikhonov regularization and total least squares. *SIAM Journal on Matrix Analysis and Applications*, 21(1):185–194, 1999.

[23] Gene H Golub and Charles F Van Loan. Matrix computations, johns hopkins u. *Math. Sci., Johns Hopkins University Press, Baltimore, MD*, 1996.

[24] Emilie M Gray and Timothy J Bradley. Evidence from mosquitoes suggests that cyclic gas exchange and discontinuous gas exchange are two manifestations of a single respiratory pattern. *Journal of Experimental Biology*, 209(9):1603–1611, 2006.

[25] Berlizé Groenewald, Stefan K Hetz, Steven L Chown, and John S Terblanche. Respiratory dynamics of discontinuous gas exchange in the tracheal system of the desert locust, schistocerca gregaria. *Journal of Experimental Biology*, 215(13):2301–2307, 2012.

[26] Per Christian Hansen. *Discrete Inverse Problems: Insight and Algorithms*. SIAM, 2010.

[27] Jon F Harrison. Ventilatory mechanism and control in grasshoppers. *American Zoologist*, 37(1):73–81, 1997.

[28] Jon F Harrison, James S Waters, Arianne J Cease, John M VandenBrooks, Viviane Callier, C Jaco Klok, Kimberly Shaffer, and John J Socha. How locusts breathe. *Physiology*, 2013.

[29] Erica C Heinrich, Matthew J McHenry, and Timothy J Bradley. Coordinated ventilation and spiracle activity produce unidirectional airflow in the hissing cockroach, gromphadorhina portentosa. *Journal of Experimental Biology*, 216(23):4473–4482, 2013.

[30] Joao P Hespanha. *Linear Systems Theory*. Princeton University Press, 2018.

[31] Stefan K Hetz and Timothy J Bradley. Insects breathe discontinuously to avoid oxygen toxicity. *Nature*, 433(7025):516–519, 2005.

[32] B. Hunt. A theorem on the difficulty of numerical deconvolution. *IEEE Transactions on Audio and Electroacoustics*, (106):640–650, 1972.

[33] Reinhold Hustert. Neuromuscular coordination and proprioceptive control of rhythmical abdominal ventilation in intact*Locusta migratoria migratorioides*. *Journal of Comparative Physiology*, 97(2):159–179, 1975.

[34] Eva Kanso and Paul K Newton. Passive locomotion via normal-mode coupling in a submerged spring-mass system. *Journal of Fluid Mechanics*, 641:205, 2009.

[35] Paul Kestler. Respiration and respiratory water loss. In *Environmental Physiology and Biochemistry of Insects*, pages 137–183. Springer, 1984.

[36] Robert Krasny. Desingularization of periodic vortex sheet roll-up. *Journal of Computational Physics*, 65(2):292–313, 1986.

[37] Robert Krasny. Computation of vortex sheet roll-up in the trefftz plane. *Journal of Fluid Mechanics*, 184:123–155, 1987.

[38] George V Lauder, Jeanette Lim, Ryan Shelton, Chuck Witt, Erik Anderson, and James L Tangorra. Robotic models for studying undulatory locomotion in fishes. *Marine Technology Society Journal*, 45(4):41–55, 2011.

[39] GW Lewis, PL Miller, and PS Mills. Neuro-muscular mechanisms of abdominal pumping in the locust. *Journal of Experimental Biology*, 59(1):149–168, 1973.

[40] John RB Lighton. Discontinuous gas exchange in insects. *Annual Review of Entomology*, 41(1):309–324, 1996.

[41] John RB Lighton. 'Instantaneous'metabolic measurement. *Journal of Experimental Biology*, pages 1605–1606, 2012.

[42] JRB Lighton and LG Halsey. Flow-through respirometry applied to chamber systems: pros and cons, hints and tips. *Comparative Biochemistry and Physiology Part A: Molecular & Integrative Physiology*, 158(3):265–275, 2011.

[43] FH McCutcheon. The respiratory mechanism in the grasshopper. *Annals of the Entomological Society of America*, 33(1):35–55, 1940.

[44] PL Miller. Respiration in the desert locust: II. the control of the spiracles. *Journal of Experimental Biology*, 37(2):237–263, 1960.

[45] Nikolaĭ Muskhelishvili and Jens Rainer Maria Radok. *Singular integral equations: boundary problems of function theory and their application to mathematical physics*. Courier Corporation, 2008.

[46] Arnold Neumaier. Solving ill-conditioned and singular linear systems: A tutorial on regularization. *SIAM Review*, 40(3):636–666, 1998.

[47] Roland Parkes, Lewis G Halsey, Anthony J Woakes, Roger L Holder, and Patrick J Butler. Oxygen uptake during post dive recovery in a diving bird *Aythya fuligula*: implications for optimal foraging models. *Journal of Experimental Biology*, 205(24):3945–3954, 2002.

[48] Hodjat Pendar. Input estimation of systems with large dataset. *https://github.com/TheSochaLab/Extended-Tikhonov-and-Dimension-Reduction-methods-for-data-recovery.*

[49] Hodjat Pendar. *The mechanical linkage of abdominal movements and the respiratory system in beetles*. PhD thesis, Virginia Polytechnic Institute and State University, 2014.

[50] Hodjat Pendar and John J Socha. Estimation of instantaneous gas exchange in flow-through respirometry systems: a modern revision of Bartholomew's Z-transform method. *PloS one*, 10(10):e0139508, 2015.

[51] Hodjat Pendar, John J Socha, and Julianne Chung. Recovering signals in physiological systems with large datasets. *Biology open*, 5(8):1163–1174, 2016.

[52] Howard A Schneiderman. Discontinuous respiration in insects: role of the spiracles. *The Biological Bulletin*, 119(3):494–528, 1960.

[53] Howard A Schneiderman and Alan N Schechter. Discontinuous respiration in insects—v. pressure and volume changes in the tracheal system of silkworm pupae. *Journal of Insect Physiology*, 12(9):1143–1170, 1966.

[54] Thomas G Shelton and Arthur G Appel. Carbon dioxide release in *Coptotermes formosanus* shiraki and *Reticulitermes flavipes* (kollar): effects of caste, mass, and movement. *Journal of insect physiology*, 47(3):213–224, 2001.

[55] Ratnesh K Shukla and Jeff D Eldredge. An inviscid model for vortex shedding from a deforming body. *Theoretical and Computational Fluid Dynamics*, 21(5):343, 2007.

[56] John J Socha, Wah-Keat Lee, Jon F Harrison, James S Waters, Kamel Fezzaa, and Mark W Westneat. Correlated patterns of tracheal compression and convective gas exchange in a carabid beetle. *Journal of Experimental Biology*, 211(21):3409–3420, 2008.

[57] Ogata H. Katayose Y. Tokuyama, K. and M. Satoh. Algorithm for transient response of whole body indirect calorimeter: deconvolution with a regularization parameter. *Journal of Applied Physiology*, (106):640–650, 2009.

[58] Gennadii M Vainikko. The discrepancy principle for a class of regularization methods. *USSR Computational Mathematics and Mathematical Physics*, 22(3):1–19, 1982.

[59] Johannes D Veldhuis, Mark L Carlson, and Michael L Johnson. The pituitary gland secretes in bursts: appraising the nature of glandular secretory impulses by simultaneous multiple-parameter deconvolution of plasma hormone concentrations. *Proceedings of the National Academy of Sciences*, 84(21):7686–7690, 1987.

[60] Torkel Weis-Fogh. Respiration and tracheal ventilation in locusts and other flying insects. *Journal of Experimental Biology*, 47(3):561–587, 1967.

[61] Ralph A Willoughby. Solutions of ill-posed problems (an tikhonov and vy arsenin). *SIAM Review*, 21(2):266, 1979.

[62] AJ Woakes and PJ Butler. Swimming and diving in tufted ducks, aythya fuligula, with particular reference to heart rate and gas exchange. *Journal of Experimental Biology*, 107(1):311–329, 1983.

[63] T Wu. Hydromechanics of swimming propulsion. Part 1. Swimming of a two-dimensional flexible plate at variable forward speeds in an inviscid fluid. *Journal of Fluid Mechanics*, 46(2):337–355, 1971.